ENERGY HARVESTING FOR PARAFOIL AND PAYLOAD AIRCRAFT SYSTEMS

A Dissertation
Presented to
The Academic Faculty

by

Matthew R. Dowling

In Partial Fulfillment
of the Requirements for the Degree
Master of Science in the
Woodruff School of Mechanical Engineering

Georgia Institute of Technology
December 2017

ENERGY HARVESTING FOR PARAFOIL AND PAYLOAD AIRCRAFT SYSTEMS

Approved by:

Dr. Mark Costello, Advisor
School of Mechanical Engineering
Georgia Institute of Technology

Dr. Jonathan Rogers
School of Mechanical Engineering
Georgia Institute of Technology

Dr. Lakshmi Sankar
School of Aerospace Engineering
Georgia Institute of Technology

Date Approved: November 10, 2017

ACKNOWLEDGEMENTS

I would like to take this opportunity to acknowledge and thank a few of the many people who have helped me along the way. First, I would like to thank the past and present members of the Center for Advanced Machine Mobility at Georgia Tech for their willingness to brainstorm new ideas, proofread seemingly endless chapters, and generally help in any way possible. In particular, I would like to acknowledge my advisor, Dr. Costello for his support, guidance, and continual encouragement.

I would also like to acknowledge the Natick Soldiers Research, Development, and Engineering Center for their financial support and enthusiasm during this project, especially Dr. Gregory Noetscher, the point-of-contact and the contract manager for this project.

Finally, I wish to acknowledge all of the love and support I have received from my friends and family. Their constant motivation, willingness to deal with me working odd hours, and much needed distractions were what made this thesis possible.

TABLE OF CONTENTS

LIST OF TABLES

LIST OF FIGURES

LIST OF SYMBOLS AND ABBREVIATIONS

A	ROTOR CROSS SECTIONAL AREA
a	AXIAL INDUCTION FACTOR
a'	ANGULAR INDUCTION FACTOR
α	ANGLE OF ATTACK
B	NUMBER OF BLADES PER ROTOR
c	CHORD
C_D	COEFFICIENT OF DRAG
C_L	COEFFICIENT OF LIFT
C_P	COEFFICIENT OF POWER
C_T	LOCAL THRUST COEFFICIENT
dQ	INCREMENTAL AMOUNT OF TORQUE PRODUCED BY EACH BLADE ELEMENT
F	TIP LOSS FACTOR
i	INDEX ALONG THE ROTOR

LIST OF SYMBOLS AND ABBREVIATIONS CONT.

j	ITERATION INDEX
K_T	MOTOR TORQUE CONSTANT
λ	TIP SPEED RATIO (TSR)
λ_r	LOCAL TIP SPEED RATIO
φ	RELATIVE WIND ANGLE
Q	TORQUE GENERATED BY THE ROTOR
σ'	BLADE SOLIDITY
θ_P	LOCAL PITCH ANGLE
θ_T	LOCAL TWIST ANGLE

SUMMARY

Guided airdrop systems offer an efficient and reliable means of delivering payloads to remote or hard-to-access locations. Utilizing a set of sensors and actuators, the Airborne Guidance Unit (AGU) intelligently controls the aircraft to a desired impact point (IP). These onboard electronics are powered using high-power-density batteries such as Lithium Polymer or Nickel Metal Hydride batteries. A logistics issue for guided airdrop systems is maintaining these batteries inside the AGU so that when the system is deployed, the batteries are adequately charged and are able to provide the requisite power to the system. It is typical for a guided airdrop system to be packed and readied for use well before deployment leading to non-negligible battery self-discharge. This necessitates a process to monitor battery life and recharge the systems after a certain time interval.

This paper explores using a small-scale wind energy harvesting system to provide the necessary power for the onboard electronics and actuation for a guided airdrop system. Sizing studies are reported to estimate the required scale of both the turbine rotor and generator. Using this information, a full-scale AGU with an integrated twin horizontal axis wind turbine system was designed, fabricated, and tested in a wind tunnel to determine the system's viability. Results indicate that a 0.33 m diameter turbine system can generate over 3.7 W of continuous power at a wind speed of 8 m/s. This is sufficient to power low-power consumption guided airdrop systems, such as a bleed air actuated system.

CHAPTER 1. INTRODUCTION

In recent years, precision guided airdrop systems have become an increasingly popular method of delivering payloads to hard-to-access locations such as areas affected by a natural disaster or active combat zones. Prior to the advent of guided parafoil technology, unguided parafoils were the primary mechanisms of delivering payloads to areas where conventional transportation was not suitable. To ensure accuracy for unguided systems, the aircraft transporting the payload must fly by the designated impact point (IP) twice, the first time to estimate the wind field surrounding the IP and the second to drop the payload. Additionally, the aircraft must travel at an abnormally low altitude, typically around 2,000 feet, to mitigate the effect of error in the wind field estimate [1]. Both practices are potentially dangerous and susceptible to large deviations in payload accuracy.

To increase the payload accuracy while alleviating these safety concerns, guided precision airdrop systems were developed. Guided airdrop systems make use of an Airborne Guidance Unit (AGU) which uses sensor measurements such as GPS, rate gyros, barometers, and magnetometers to actively navigate the payload to the IP. The sensor measurements are incorporated into a guidance, navigation, and control (GNC) algorithm which utilizes lateral and longitudinal control to adjust the parafoil's left/right turn radius and the glide slope. The GNC eliminates the need to pass by the IP to develop an estimate of the wind field and allows soldiers to accurately and safely drop the payload from an altitude of approximately 25,000 feet [2].

1.1 Overview of Guided Airdrop Systems

A typical guided airdrop system consists of three major sections: the parafoil, the payload, and the Airborne Guidance Unit (AGU) (Figure 1). The AGU is the component

which separates a guided airdrop system from its unguided counterpart, serving to house the sensors, actuators, microprocessors, and batteries responsible for controlling the system. Guided airdrop systems make use of sensors such as GPS, accelerometers, gyroscopes, magnetometers, and barometers to drive the actuators which steer the system towards a designated landing zone. The integration of these sensors and their control mechanisms has greatly enhanced the landing accuracy of parafoil and payload aircraft.

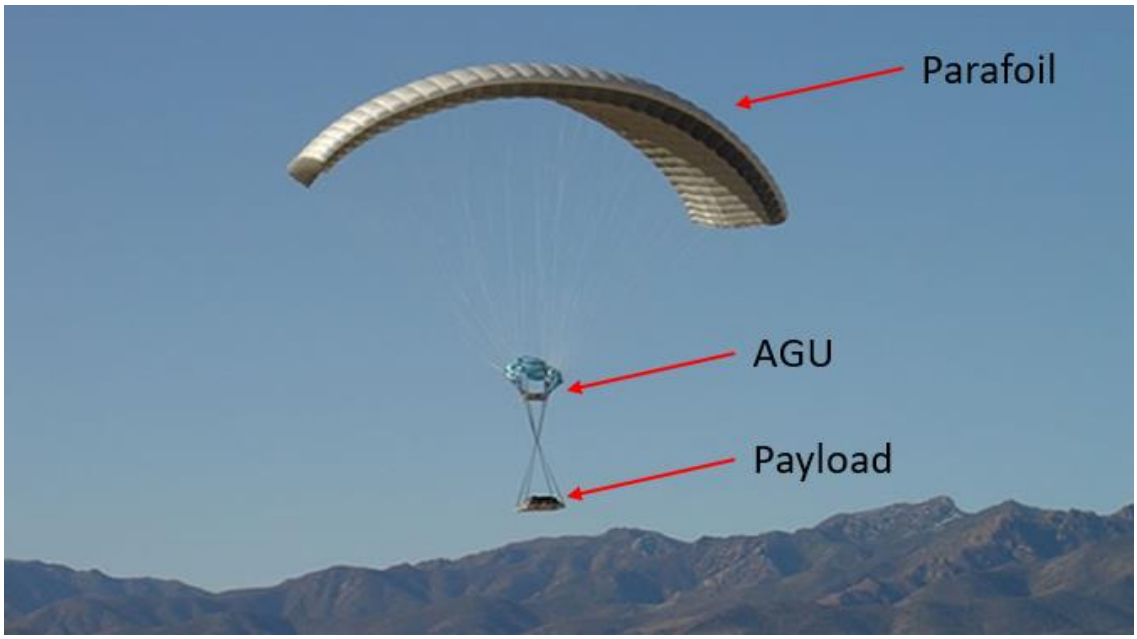

Figure 1: Dragonfly Guided Airdrop System [3]

In a practical setting, guided airdrop systems are packed and readied for flight well in advance of their use. During the time between packing and deployment, batteries inside the AGU self-discharge at a nominal rate. For example, the typical self-discharge rates of common rechargeable battery cells are as follows: nickel-cadmiuim (15-20% per month), nickel metal hydride (20-30% per month), and lithium (5-10% per month) [4]. If the guided airdrop system is unattended for too long a period after packing, the batteries can lose their

charge resulting in possible failure of the AGU and the flight. Thus, these systems must be monitored and maintained at regular intervals to ensure batteries have the necessary charge for proper operation. This represents an unwanted logistics and maintenance burden for soldiers.

1.2 Review of Previous Small-Scale Wind Energy Harvesting Systems

An alternative to powering guided airdrop systems with batteries is to use an onboard, small-scale wind energy harvesting system. There are a myriad of ways to harness wind energy on a small-scale such as vertical and horizontal axis wind turbines, aerodynamic flutter, vortex induced vibrations, and galloping [5-10]. While many industries and researchers have examined different methods of harnessing wind energy, by far the most common device is the horizontal axis wind turbine (HAWT). Federspiel and Chen used a windmill to supply an air powered sensor using a commercially available fan blade as a rotor and a low-speed, three-phase, brushless DC servomotor as a generator. They rectified the AC current using a three-phase bridge constructed from six diodes and achieved efficiency levels of less than 10% while creating 7-28 mW in 2.5 m/s winds and a resistive load of 100 Ω [11]. Rancourt, Tabesh, and Frechette evaluated a micro windmill with a diameter of 4.2 cm and achieved efficiency levels of 1.5% at a wind speed of 5.5 m/s and 9.5% at 11.8 m/s. The generated power varied between 2.4 mW and 130 mW respectively [12]. Xu, Yuan, Hu, and Qiu used a miniature wind turbine for powering wireless sensors consisting of a 7.6 cm plastic propeller blade as a rotor and a permanent magnet DC motor as a generator. With wind speeds of 4.5 m/s, they generated 18 mW of power at an efficiency of 7.6% [13]. An overview of the results from similar small-scale HAWTs is provided in Table 1.

Table 1: Small-Scale Wind Turbine Examples

Authors	Number of Blades	Rotor Diameter [cm]	Air Speed [m/s]	Maximum Power [mW]	Maximum Efficiency	Power Desnity [mW/cm^2]
Federspiel and Chen (2003) [11]	4	10.0	2.5	8	10%	0.10
Holmes et al. (2005) [14]	24	0.75	40.0	1.1	0.4%	2.26
Hirahara et al. (2004) [15]	4	5.0	9.4	2965	28%	1.51
Priya et al. (2007) [16]	12	10.2	4.4	5	1.1%	0.06
Rancourt et al. (2007) [12]	3	4.2	11.8	130	9.5%	9.39
Xu et al. (2010) [13]	4	7.6	4.5	18	7.6%	0.40
Carli et al. (2010) [17]	4	6.3	4.4	10		0.32
Sardini et al. (2011) [18]	2	6.5	9.0	45	13-15%	1.36

Danick et al. performed an analysis comparing the efficiency of several small-scale wind energy devices, plotting efficiencies versus wind speed: solid marks indicate wind turbines, open marks indicate vortex shedding devices, and hash marks indicate flutter/galloping devices (Figure 2) [19]. It is clear that no current small-scale wind energy harvesting systems approach the theoretical Betz limit of 59.3% and that small-scale turbines typically have a much higher overall efficiency than other mechanisms.

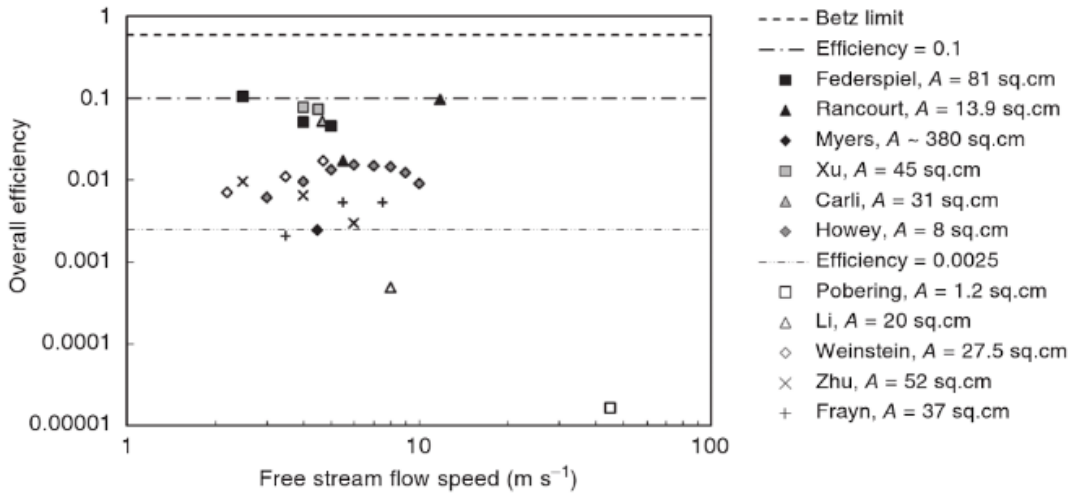

Figure 2: Efficiency vs Wind Speed for a Variety of Micro-Wind Energy Harvesting Devices [19]

For a parafoil canopy to be properly inflated, guided airdrop systems must fly through the atmosphere at a certain minimum airspeed. Depending on the particular system, guided airdrop systems typically have an airspeed of 6-13 m/s. Thus, a guided airdrop system has access to a 6-13 m/s wind stream during the entirety of its flight. A HAWT immersed in such a wind field can extract a percentage of this wind energy.

It is well known that the maximum power extraction potential of an ideal rotor in a wind stream behaves according to Eq. (1).

$$P_W = \frac{1}{2}\rho A U^3 C_P \tag{1}$$

In the above equation; ρ is the density of the air, A is the cross-sectional area of the rotor, U is the relative wind speed, and C_p is the coefficient of power. The theoretical limit of C_P, the Betz limit, is 0.593 and represents the maximum possible power that can be extracted

from the wind by a rotor [20]. While power coefficient levels of modern wind turbines have been trending towards this limit, only large-scale systems typically achieve a power coefficient of over 45%. At smaller scales, power coefficients usually drop dramatically due to the aerodynamic characteristics of airfoils at low Reynolds numbers. In addition, gearboxes typically have lower efficiencies at very small scales and can decrease the efficiency further by as much as 50%. Nevertheless, a significant amount of power can be harnessed from a relatively small HAWT rotor radius for the range of wind speeds experienced by guided airdrop systems (Figure 3).

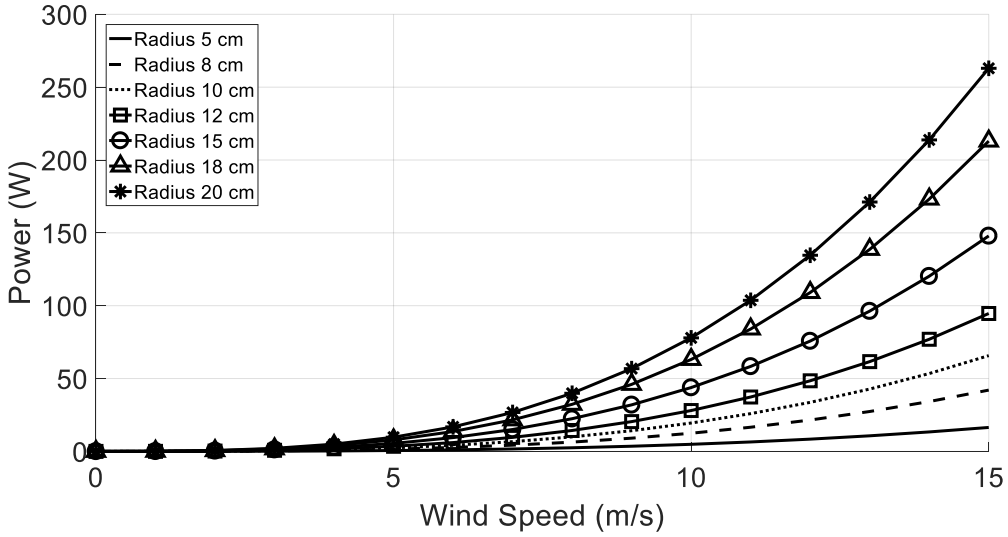

Figure 3: Extractable Power Using a Wind Turbine Operating at the Betz Efficiency vs Wind Speed for Varying Cross-Sectional Area Radii

1.3 Thesis Contributions

The objective of this thesis it to design, fabricate, and test a novel wind energy harvesting device used for powering low power consumption guided airdrop systems such

as a bleed-air actuated system. The thesis begins by describing the analysis method to design and size a HAWT system. This is followed by a detailed description of the newly designed AGU with two HAWTs integrated in the AGU structure. Finally, power extraction results from wind tunnel tests are presented for the designed system at different wind speeds, orientations, and configurations.

CHAPTER 2. WIND TURBINE SIZING STUDIES AND ANALYSIS

This chapter focuses on sizing the rotor and the generator of a horizontal axis wind turbine to meet the power requirements of a low-power consumption guided airdrop system such as the bleed air actuated system. The process of matching the optimal operating point of the aerodynamic subsystem (the rotor), the generator subsystem, and electrical subsystem is outlined.

2.1 Aerodynamic Analysis

The Betz limit analysis, described by Eq. (1), is the maximum possible power that can be extracted from the wind using a horizontal axis wind turbine (HAWT). Practically, aerodynamic inefficiencies such as wake rotation, non-ideal rotor geometry, and tip losses decrease the amount of power a turbine can extract. A typical approach to model these inefficiencies is to analyze the rotor using blade element momentum theory. This theory combines the conservation of momentum principle with blade element theory. A variant of the blade element momentum theory method presented by Manwell, McGowan, and Rogers was used to analyze the behavior of a selected rotor [21]. They outline an iterative solver for simulating wind turbine aerodynamics at a single wind speed for a desired tip speed ratio. The tip speed ratio of a rotor is defined by Eq. (2) where R is the radius of the rotor, Ω is the hub angular velocity, and U is the free stream velocity.

$$\lambda = \frac{\Omega R}{U} \tag{2}$$

The solver operates by iterating on the axial and angular induction factors, *a* and *a'*, for each blade element. These parameters are defined by Eqs. (3) and (4) where U_1 is the free stream wind velocity, U_2 is the wind velocity at the rotor plane, ω is the rotational velocity imparted to the flow stream, and Ω is the angular velocity of the rotor. Using an optimum rotor analysis as an initial estimate for *a* and *a'* and knowledge of the airfoil's chord, twist, and lift and drag characteristics, an updated value for *a* and *a'* can be calculated for each blade element. This process continues until specified conditions are met namely, the error between iterations falls below an acceptable tolerance level and the value of the parameters have physical significance. Physical significance is defined as having all real parts and all values being positive.

$$a = \frac{U_1 - U_2}{U_1} \tag{3}$$

$$a' = \frac{\omega}{2\Omega} \tag{4}$$

The modified solver employed uses optimum rotor analysis (ideal chord and twist distributions) as an initial estimate to solve for *a* and *a'* at the midpoint of each blade element.

$$\varphi_{i,1} = \frac{2}{3}\tan^{-1}\left(\frac{1}{\lambda_{r,i}}\right) \tag{5}$$

$$a_{i,1} = \frac{1}{1 + \frac{4\sin\left(\varphi_{i,1}\right)^2}{\sigma_i' C_{L_i}\cos\left(\varphi_{i,1}\right)}} \tag{6}$$

$$a'_{i,1} = \frac{1 - 3a_{i,1}}{4a_{i,1} - 1} \tag{7}$$

$$\sigma_i' = \frac{Bc_i}{2\pi r_i} \tag{8}$$

Where φ is the relative wind angle, λ_r is the local tip speed ratio of the blade element, C_L is the coefficient of lift, and σ' is the blade solidity given by Eq. (8). In Eq. (8), c is the chord, B is the number of blades on the rotor, and r is the radius of the midpoint of the blade element. With these values, it is possible to calculate the relative wind angle and the tip loss factor, φ and F, using Eqs. (9) and (10), where R is the radius of the entire blade.

$$\tan(\varphi_{i,j}) = \frac{1 - a_{i,j}}{(1 + a'_{i,j})\lambda_{r,i}} \tag{9}$$

$$F_{i,j} = \frac{2}{\pi}\cos^{-1}\left(\exp\left[-\left\{\frac{B/2\,[1 - (r_i/R)]}{r_i/R\,\sin(\varphi_{i,j})}\right\}\right]\right) \tag{10}$$

With knowledge of the relative wind angle and the pitch angle at each section along the blade, the coefficients of lift and drag, C_L and C_D, are calculated by computing the angle of attack, α, using Eq. (11) and knowledge of the airfoil.

$$\alpha_{i,j} = \varphi_{i,j} - \theta_{p,i} \tag{11}$$

The local thrust coefficient can then be calculated by Eq. (12).

$$C_{T,i,j} = \frac{\sigma_i'(1 - a_{i,j})^2 (C_{L,i,j}\cos(\varphi_{i,j}) + C_{D,i,j}\sin(\varphi_{i,j}))}{\sin(\varphi_{i,j})^2} \tag{12}$$

If the local thrust coefficient is less than 0.96, Eq. (13) is used to update the value of *a* according to momentum theory.

$$a_{i,j+1} = \frac{1}{1 + \frac{4F_{i,j}\sin\left(\varphi_{i,j}\right)^2}{\sigma_i' C_{L,i,j}\cos(\varphi_{i,j})}} \tag{13}$$

If the local thrust coefficient is greater than or equal to 0.96, the rotor is in the presence of a turbulent wake state. Therefore, the value of *a* is updated per the empirical model developed by Glauert [22].

$$a_{i,j+1} = \frac{1}{F_{i,j}}\left[0.143 + \sqrt{0.0203 - 0.6427\left(0.889 - C_{T,i,j}\right)}\right] \tag{14}$$

The next iteration of the angular induction factor is given by Eq. (15).

$$a'_{i,j+1} = \frac{1}{\frac{4F_{i,j}\cos(\varphi_{i,j})}{\sigma_i' C_{L,i,j}} - 1} \tag{15}$$

The error between the axial induction factors is calculated by Eq. (16). If this error is deemed to be within an acceptable tolerance, the coefficient of power can be calculated for the rotor with Eq. (17).

$$e = \frac{\sum_{i=1}^{N}\left|\left(a_{i,j+1} - a_{i,j}\right)\right|}{N} \tag{16}$$

$$C_P = \sum_{i=1}^{N} \left(\frac{8\Delta\lambda_r}{\lambda^2}\right) F_i \sin(\phi_i)^2 \left(\cos(\phi_i) - \lambda_{ri} \sin(\phi_i)\right) * \left(\sin(\phi_i) + \lambda_{ri} \cos(\phi_i)\right)[1 - \left(\frac{C_{Di}}{C_{Li}}\right) \cot(\phi_i] \lambda_{ri}^2 \quad (17)$$

It is also possible to calculate the incremental amount of torque generated by each section of the blade, where ρ is the density of the air and U is the relative wind speed.

$$dQ_i = \sigma_i' \pi \rho \left(\frac{U^2 \left(1 - a_{i,j}\right)^2}{\sin\left(\phi_{i,j}\right)^2 \left(C_{Li,j} \sin\left(\phi_{i,j}\right) - C_{Di,j} \cos\left(\phi_{i,j}\right)\right) r_i^2 R}\right) \quad (18)$$

The total torque generated by the rotor is then:

$$Q = \sum_{i=1}^{N} dQ_i \quad (19)$$

2.2 Generator Analysis

When using a permanent magnet DC generator, two main factors influence the efficiency of the system, the angular velocity of the generator and the load impedance. The angular velocity of the generator can in part be controlled via a gearbox to obtain the specific motor's optimum angular velocity. Ideally, the maximum efficiency of a DC generator occurs when the output impedance of the electrical load matches the internal impedance of the generator. At steady state, the impedance of the generator is simply the resistance of the internal windings.

To determine the efficiency of a specific generator, a DC motor can be used to drive the generator. Knowing only the stall torque and no load speed of the driving motor and

measuring the voltage into the motor, the angular velocity of the motor and the voltage out of the generator, the efficiency of the generator can be determined.

To calculate the output power of the DC motor, thus the power into the generator, Eqs. (20), (21), and (22) can be used to first calculate the torque. These equations arise from analyzing a linear approximation of the torque versus speed curve. In Eqs. (20), (21), and (22), $\frac{K_t^2}{R}$ and $\frac{K_t}{R}$ are constants specific to the selected motor, τ_s is the stall torque, ω_0 is the no load speed, V is the voltage driving the motor, and ω is the angular velocity of the motor.

$$\frac{K_t^2}{R} = \frac{\tau_s}{\omega_0} \tag{20}$$

$$\tau_s = \frac{K_t}{R} V \tag{21}$$

$$\tau = \frac{K_t}{R} V - \frac{K_t^2}{R} \omega \tag{22}$$

Once the torque has been calculated, the power output of the motor is given by Eq. (23).

$$P = \tau \omega \tag{23}$$

2.3 Example Analysis

To achieve the optimal efficiency of the system, the operating points of the aerodynamic and electrical subsystems must be matched properly. To highlight the generator-turbine matching process, an example rotor and generator are considered using the analysis method described above. The candidate rotor has 3 blades and a diameter of 0.33 m. The blades have a pitch of 0.15 m and employ a Clark Y airfoil section. The chord

distribution can be found in Table 2 and was determined by taking measurements at 9 points along one of the blades. The coefficients of lift and drag were calculated by aggregating data tables from an Xfoil solver for low angles of attack and data for the NACA 0015 at low Reynolds numbers for higher angles of attack [23]. This was deemed acceptable as typical rotors operate well below their stall point. This was verified in simulation.

Table 2: Chord Distribution of the Selected Rotor (r/R, fraction of rotor radius)

r/R	Chord, m
0.15	0.0239
0.25	0.0231
0.35	0.0235
0.45	0.0245
0.55	0.0249
0.65	0.0241
0.75	0.0240
0.85	0.0203
0.95	0.0178

Figures 4 and 5 show the effect of varying tip speed and wind velocity on the coefficient of power and the output torque for the rotor using the logic described in Chapter 2.1. For a given tip speed ratio, the generated power and torque increase as the wind speed increases while the coefficient of power remains independent of wind speed. In addition, there is a clear maximum for the coefficient of power at a tip speed ratio of 3.75. This will be the desired design point when matching the wind turbine and generator subsystems. It is also worth noting that while the aerodynamic efficiency is less than the Betz limit prediction, the wind turbine is still able to produce an appreciable amount of power. The power output for a tip speed ratio of 3.75 at 5 m/s is 2.5 W and at 9 m/s is 15 W.

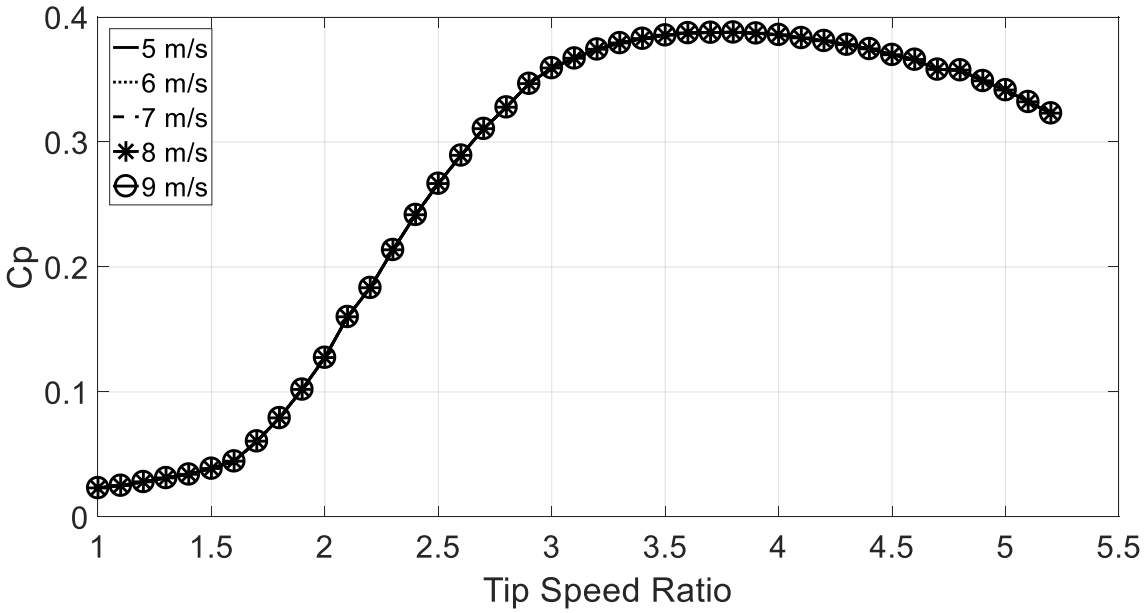

Figure 4: Coefficient of Power vs Tip Speed Ratio for the Clark-Y Airfoil from Blade Element Momentum Theory

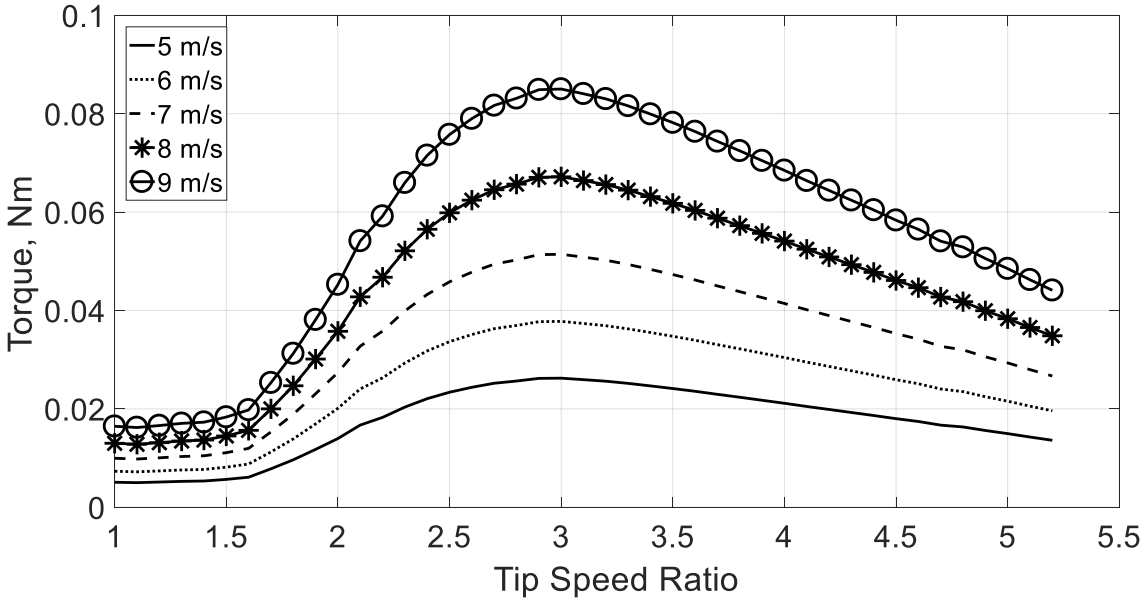

Figure 5: Torque vs Tip Speed Ratio for the Clark-Y Airfoil from Blade Element Momentum Theory

The candidate generator is a Pololu 25 mm diameter medium power gear motor with a 4:1 gear box. Efficiency of the generator was determined experimentally. Each motor was integrated with a 48 count per revolution (CPR) quadrature encoder. A microcontroller was used to convert the encoder readings of the motor shaft to angular velocity. The motor specifications list the stall torque and the no load speed for the nominal voltage, 12 V. With these two values, the torque-speed curve of the specific motor for any voltage can be approximated linearly by Eqs. (20), (21), and (22) (Figure 6). Thus, the power can be approximated using Eq. (23) (Figure 7).

To measure the output power of the generator, a simple resistive circuit was created. The voltage drop across the resistor was measured every second for one minute using a moving average filter. The sixty measurements were then averaged to calculate the voltage. The power output from the generator can be calculated using Eq. (24).

$$P_{out} = \frac{V^2}{R} \tag{24}$$

The efficiency of the motor can then be determined Eq. (25).

$$\eta = 100\ \frac{P_{out}}{P_{in}} \tag{25}$$

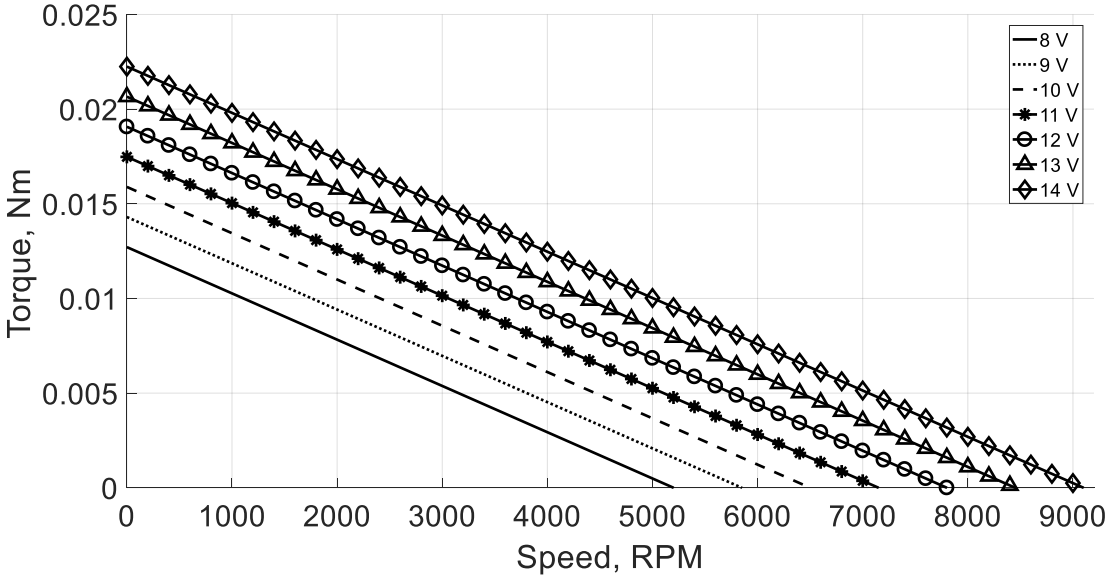

Figure 6: Torque vs Speed Curve for the Pololu 25 mm Diameter Gear Motor

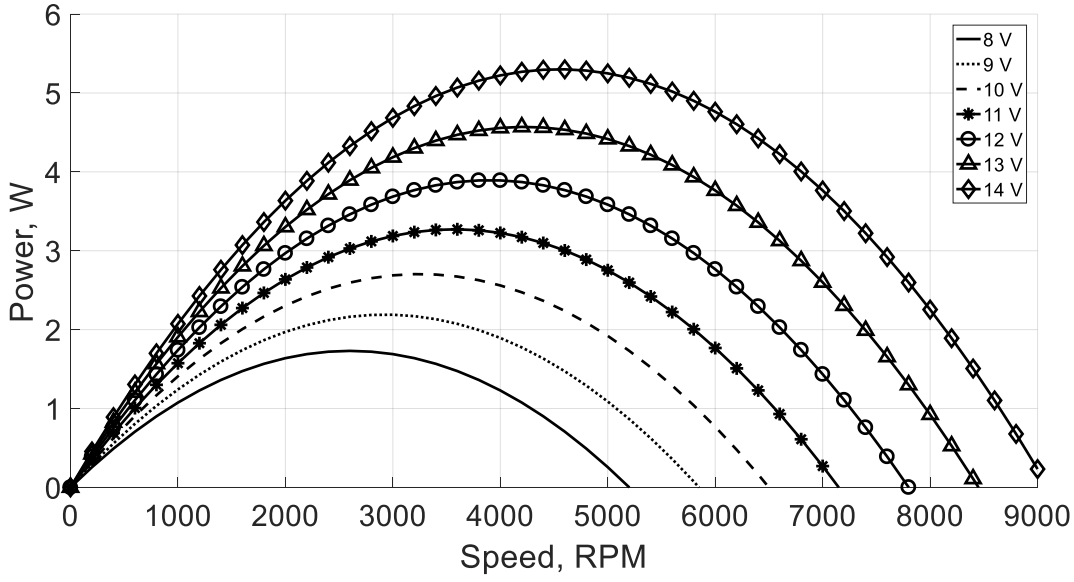

Figure 7: Power vs Speed Curve for the Pololu 25 mm Diameter Gear Motor

The efficiency of the motor was measured for resistance values of 10, 20, 30, 40, 50, 60, and 70 Ω at 100, 300, 500, 700, 900, and 1100 RPM (gear shaft velocity with a 4:1 gear ratio). The motor operates at its highest efficiency for a resistance value of 20 Ω (Figure 8). The motor's efficiency increases with speed up to 700 RPM and then begins to diminish (Figure 9). From Figure 8 andFigure 9, it is evident that the generator's efficiency is a function of both load resistance and angular velocity.

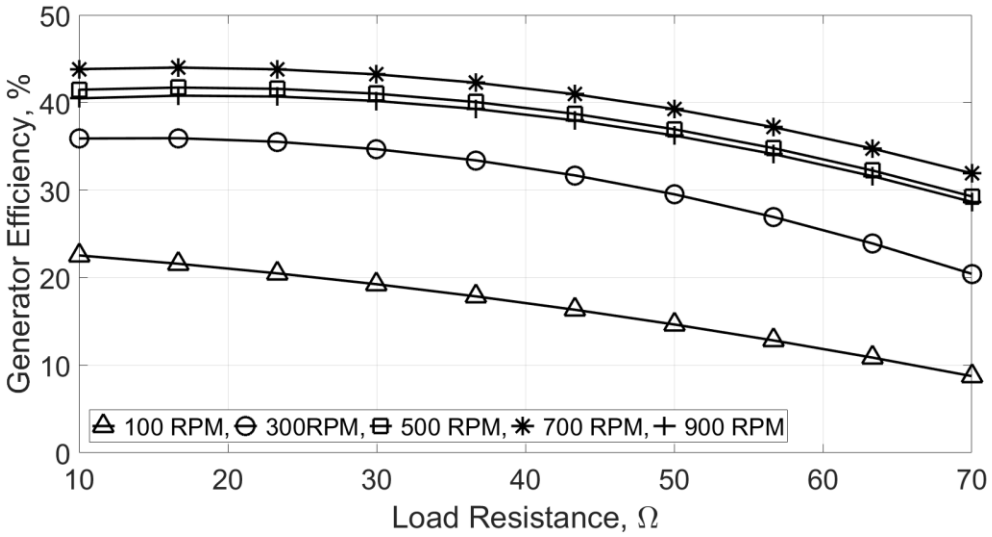

Figure 8: Second Order Polynomial Fit for Generator Efficiency vs Load Resistance for Multiple Angular Velocities

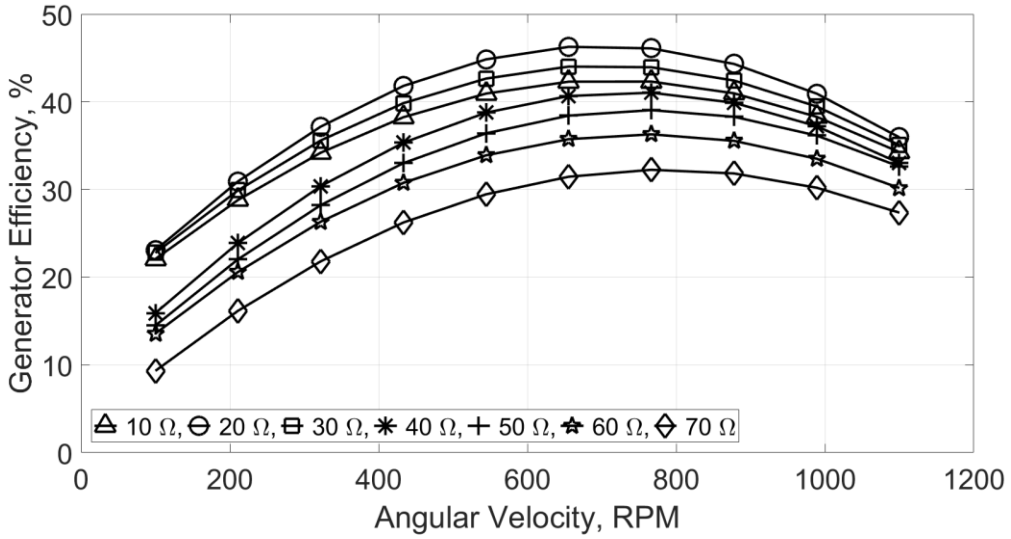

Figure 9: Second Order Polynomial Fit for Generator Efficiency vs Angular Velocity for Multiple Load Resistances

To harness the maximum possible energy using a wind turbine, the operating point of each individual subsystem must be matched to optimize system performance. A flow chart of the interaction between the components is shown below (Figure 10).

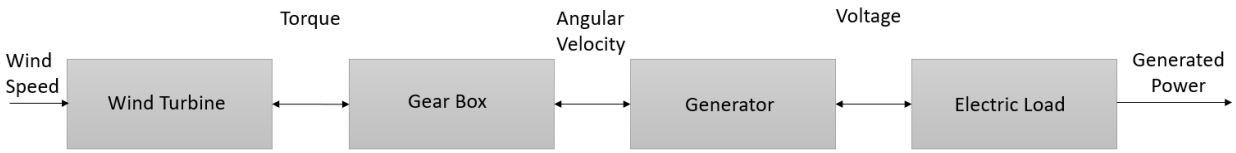

Figure 10: Subsystem Flow Chart

Ideally, the system would operate at each subsystem's most efficient point. However, due to the complex interactions between the subsystems, this is not always possible. Given any three components, the fourth component can be varied to determine a local maximum efficiency. For instance, for a selected rotor, gear box, and generator, the electrical load

can be varied to find the maximum efficiency of this configuration. In practice, elements such as the rotor and generator are selected based on other design constraints, such as size or cost. This leads to varying only the gear box and electrical load to determine the global maximum efficiency of the system.

CHAPTER 3. DESIGN OF THE ENERGY HARVESTING SYSTEM

The AGU design incorporates a wind energy harvesting system into a compact housing that contains actuators and electronics. The system provides sufficient power for a low-power consumption guided airdrop system such as a bleed air actuated system while roughly maintaining the size of current AGUs. Two separate designs are outlined, one for the initial prototype which was tested in the low-turbulence wind tunnel at the Georgia Institute of Technology and one for a full-scale system which is designed specifically for flight testing.

3.1 Prototype Design

The design is comprised of two major subassemblies, the turbine system and the housing. The turbine system is responsible for generating the power required by the onboard electronics and actuators. The housing has three major functions: to hold all onboard electronics and actuators, to protect these components in the event of a high impact landing, and to act as an attachment point to the parafoil and the payload. The AGU system can be seen in Figure 11.

The turbine system, shown in detail below, consists of a propeller, a permanent magnet DC machine to act as a generator, a gearbox, a motor mount, and a shaft coupler (Figure 12). The propeller was selected based on initial sizing estimates using blade element momentum theory and examining available purchasing options. Two medium-power Pololu 25 mm diameter gear motors are used as generators. This motor was selected as it had desirable characteristics, such as a low start-up torque and compactness. Moreover, the Pololu 25 mm diameter gear motor is also cost efficient. While the cost of the system was

not one of the primary design objectives for the prototyping stage, for this design to be practically implemented onto existing guided airdrop systems, it must be able to be produced cost effectively. More information on the rotor and generator can be found in CHAPTER 2.

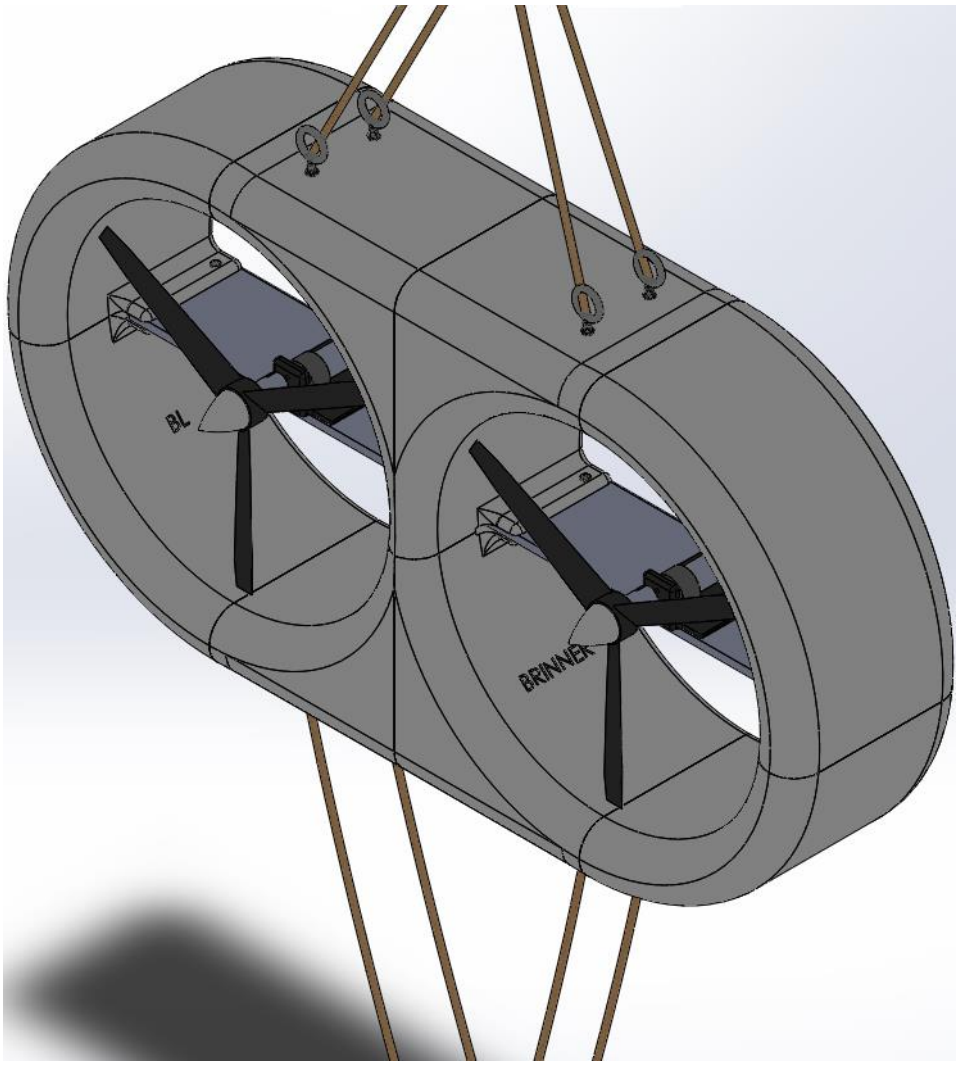

Figure 11: Self-Powered AGU System

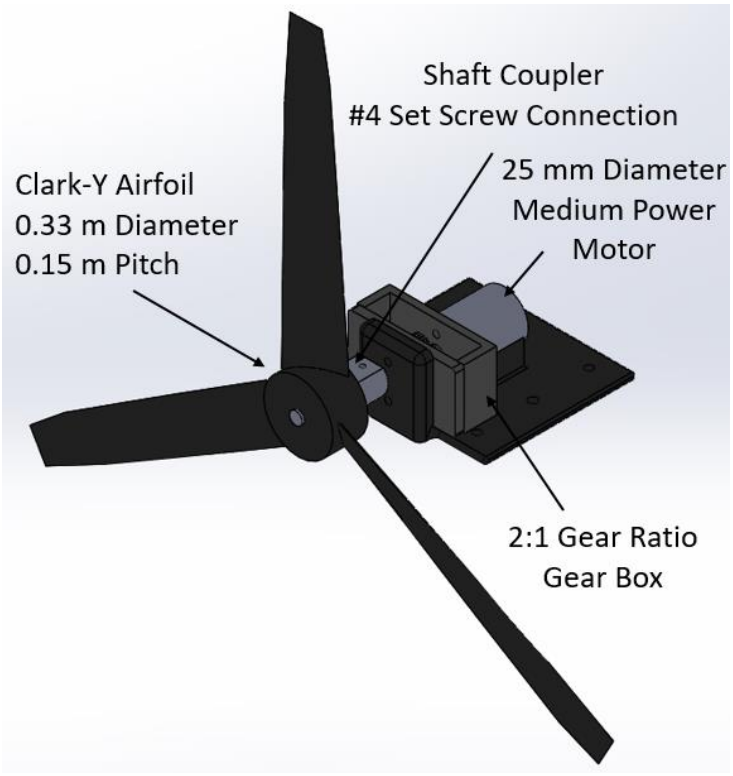

Figure 12: Turbine System Subassembly

The gear box, shown in Figure 13, was constructed based on the provided pinion on the generator's output shaft. Initial wind tunnel testing suggested that the standard gear ratio of 9.68:1 increased the generator's load torque to a point where the rotor could not spin near the predicted optimum tip speed ratio resulting in low overall efficiency. Therefore, a custom gear box was created to analyze several different gear ratios. To fully optimize the system, the load impedance can be varied over a spectrum of gear ratios. The maximum efficiency for each gear ratio/impedance combination can be compared to determine the optimal configuration. This study examines gear boxes with only one pinion-gear combination due to the large role that gear friction can play in small-scale energy harvesting systems: each additional spur gear would only increase the system's total losses. Gear ratios of 2:1, 3:1, and 4:1 were examined.

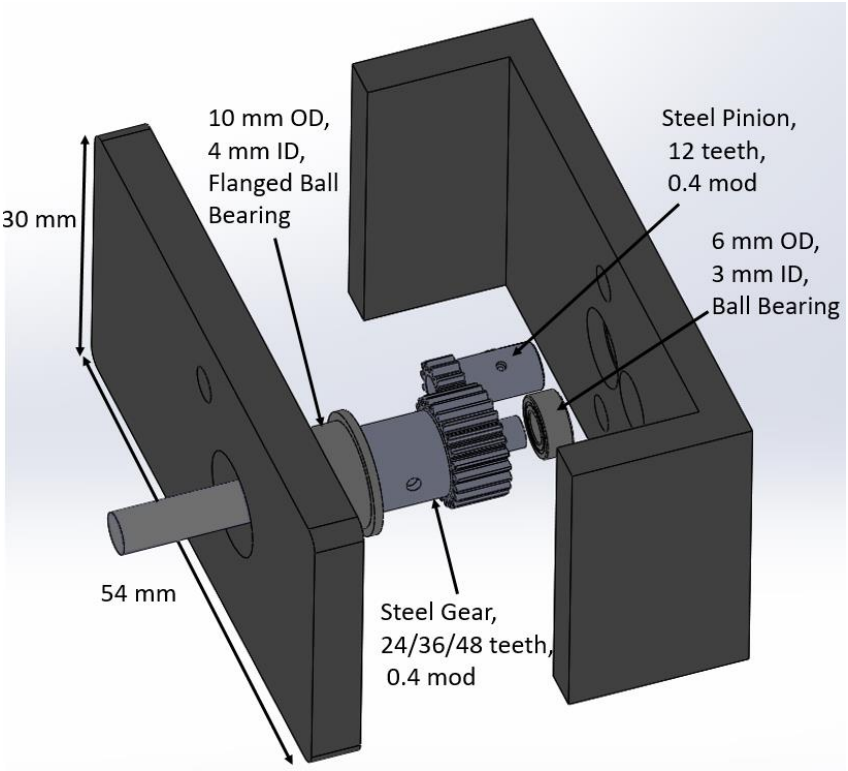

Figure 13: 2:1 Ratio Gearbox, Exploded View

The motor mount used for this system was designed from an existing mount created specifically for the Pololu 25 mm diameter motor. The mount was streamlined to provide more aerodynamic efficiency.

The shaft coupler is a custom, 3D printed part connecting the male output shaft of the motor to the female bore of the propeller. A #4 set screw is used to maintain the connection between the motor shaft and the coupler, while the propeller hub and the coupler are epoxied together. The housing was designed to minimize the projected area seen by the wind while maintaining structural integrity and offering protection to the energy harvesting and control systems. This subassembly was separated into 8 total parts for ease of

manufacturing. All 8 of these parts are mechanically connected using #6 screws through a solid sheet of PVC that spans the entire AGU.

To facilitate the experimental setup in the wind tunnel, eight eye screws were implanted into the inner portions of the housing, four on the top surface and four on the bottom. This was accomplished by press fitting threaded inserts into the 3D printed parts and threading the eye screws into these features. As the top four eye screws needed to carry all the weight of the system, epoxy was added to enhance the strength of the press-fit connection between the threaded insert and the housing. The four screws on the bottom were utilized for stability purposes and will later serve to connect the AGU to the payload during flight.

3.2 Flight Test Design

To ensure that the revised AGU can handle the rigors of flight testing, a separate design was created specifically for full-scale flight testing. There are two significant modifications that must be made from the wind tunnel AGU design. The first is that the flight test design must be sufficiently durable to operate under the increased loads seen during flight testing. The second is the AGU must be adapted for different nominal flight conditions. Where the wind flow in the wind tunnel tests was perpendicular to the suspended AGU, the wind flow during a flight test will be approximately at the glide slop angle.

The first modification made to the AGU design is to strengthen the subassemblies to prevent premature failure due to the increased loads the AGU experiences during a flight test, specifically during deployment. When the guided airdrop system is deployed, the canopy, AGU, payload connection point, and tethers all experience a significant force due to the impulse of the canopy opening. In practice, different methods are used to reduce high

shock openings such as mechanical sliders (mini drag chute) and stiffening elements embedded in the tethers to allow some flexibility. Even with these mechanisms in place, the 3D printed housing cannot withstand the opening forces. To combat this, each part of the flight test design's housing subsystem will be machined out of 6061 Aluminum due to its strength, ease of manufacturing, and corrosive properties. The added strength of the Aluminum also allows the top and bottom surface of the inner portions of the AGU to be directly tapped rather than using the press-fit threaded insert used in the wind tunnel design, increasing the strength of the connection. The revised tether to AGU connection can be seen in Figure 14.

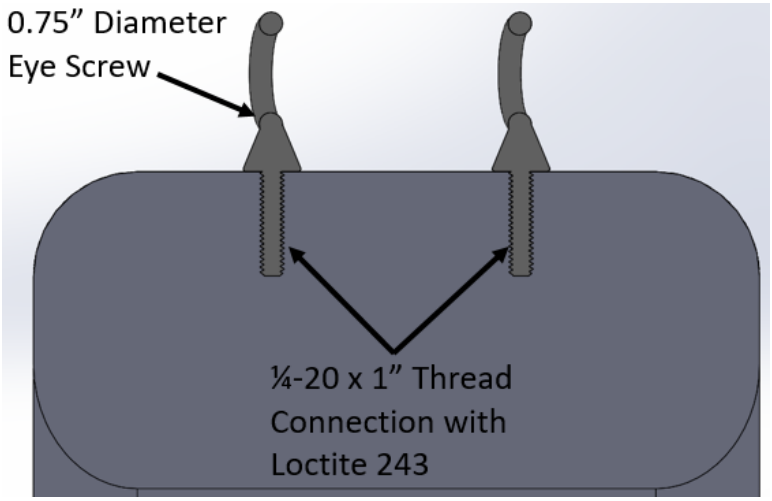

Figure 14: Cross Section of the Flight Test Design Tether to AGU Connection

Due to the possible higher wind speeds, turbulence, and rapidly changing angles of relative wind, the turbine subsystem must be bolstered as well. As with the housing assembly, the previously 3D printed parts, namely the shaft coupler and motor mount, will

now be machined out of 6061 Aluminum. The reasons for this are twofold: to increase the strength of the parts and to machine the parts to a much tighter tolerance than most 3D printers can produce. The decreased tolerance on the shaft coupler's bore diameter and the motor mount's supporting structure radius will decrease harmful vibration throughout the system.

The second significant modification, altering the design to better incorporate nominal flight conditions, was made to ensure that the turbine system was operating at its optimal efficiency throughout the flight. Specifically, in the wind tunnel, the ambient airflow was perpendicular to the face of the AGU. However, during flight testing, the angle of relative wind will not be perpendicular to the face of the AGU, it will be the resultant vector of the velocity vector of the guided airdrop system and the velocity vector of the wind. While it is difficult to predict the wind velocity vector for every flight, the velocity vector of the guided airdrop system is fairly constant for a given system. This velocity vector is known as the glide slope and is the ratio of forward flight velocity to the descent rate. Typical lightweight guided airdrop systems have a glide slope of approximately 4. With no atmospheric wind velocity, this would equate to a 14 degree relative wind angle. The wind tunnel and flight test relative wind angle conditions are shown below in Figure 15.

To optimize the flight test design for the predicted relative wind angle, the rotor axis is tilted 14 degrees to face the oncoming wind. The redesigned AGU with the offset rotor rotational axis is shown in Figure 16.

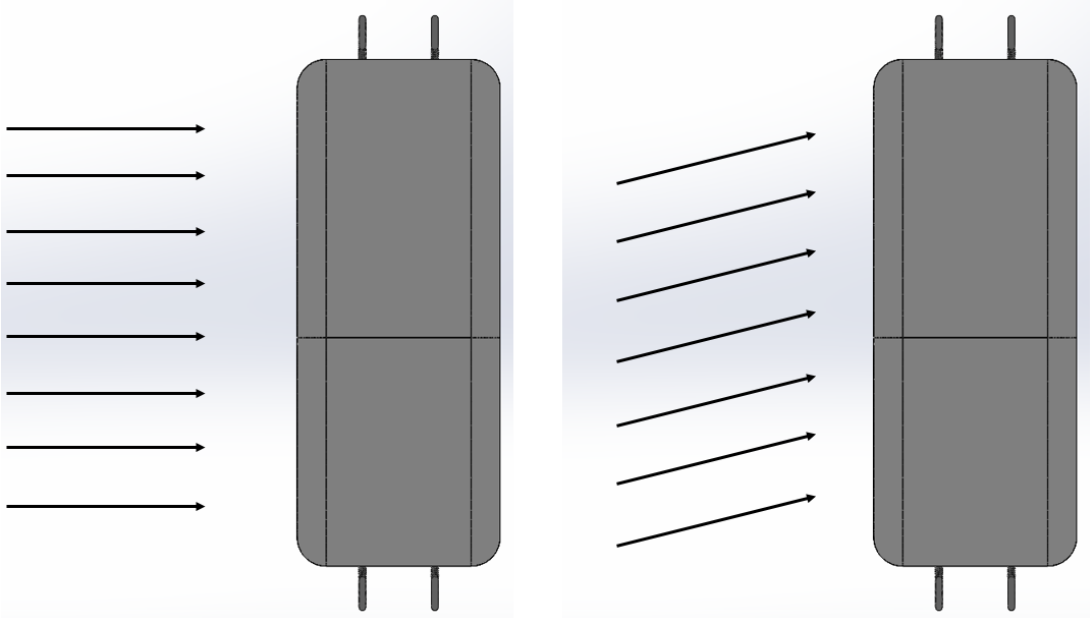

Figure 15: Ambient Wind Streamlines for a) Wind Tunnel Conditions and b) Flight Test Conditions Assuming no Atmospheric Wind Velocity or Turbulence

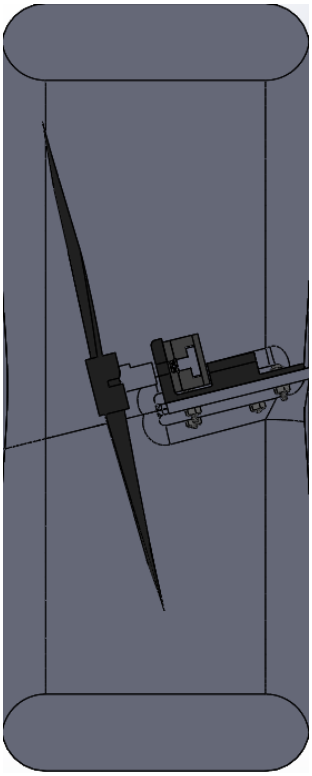

Figure 16: Cross Section of the Flight Test Design Rotor Axis

CHAPTER 4. WIND TUNNEL TEST RESULTS

This chapter outlines the impetus, methodology, and results for the wind tunnel tests of the full-scale AGU. The results are divided into two sections for clarity. The first section examines the optimal configuration of the system by varying gear ratio and load impedance. The second analyzes the performance of the system at varying angles of attack and side slip.

4.1 Optimal Configuration Analysis

The power generated by the system at a given wind speed can be adjusted by matching the operating point of the aerodynamic and electrical subsystems. This section will focus on determining the optimum operating point of the system for three gear ratios by varying the output impedance.

4.1.1 Methodology

A series of tests were conducted to determine the optimal configuration of system. Each of these experiments took place in the exhaust section of the low turbulence wind tunnel at the Georgia Institute of Technology. The revised AGU was suspended from the roof of the wind tunnel using 500 lb parafoil chord. The parafoil cord was tied from each of the eye screws into a confluence point and then tied directly above to the roof of the wind tunnel. To improve rotational stability about the pitch axis, cord from the bottom four eye screws was tied into a confluence point and then attached to the floor of the test section. To mitigate any unwanted side slip, the cord was threaded through gaps in between the outer upper and lower surfaces and tied off to the sides of the wind tunnel. The full experimental setup can be seen in Figure 17.

Figure 17: Wind Tunnel Experimental Setup

To accurately measure power, an MSP432 microcontroller read voltage and angular velocity measurements every half second for four minutes. The voltage readings were measured using the ADC feature of the microcontroller and were passed through a low-pass filter with a cutoff frequency of 0.15 Hz. The generator was equipped with a 48 CPR quadrature encoder to provide the angular velocity measurements. The final 280 data points of the filtered voltage and angular velocity were averaged to find the typical voltage and angular velocity for the specific test. Each test was conducted three times and the average of the three tests was used as the final value. This process mitigated the effect that error could have on the measurements. Power generated was calculated using Eq. (23).

Each test was conducted in three stages: the preparation stage, the forward progression stage, and the reverse progression stage. The testing was divided into the forward and reverse progression stages to visualize any possible hysteresis in the system. During the preparation phase, the resistance value was tuned to within ±0.5 Ω of the desired value, the AGU was tied firmly in place to ensure no unintentional movement occurred during the test, and the microcontroller was attached to the generator and encoder. The resistance values were determined in an iterative process beginning at 10 Ω and increasing until a clear trend became apparent.

The forward progression stage was designed to test the wind speeds in an increasing order, starting at 4.5 m/s and ramping up to 8 m/s. This range was selected to analyze practical wind speeds for a light weight parafoil-payload aircraft. The energy harvesting system must be able to power the control and actuation systems even if it is only exposed to slower wind speeds during flight. To begin the test, the wind tunnel was activated and the wind speed was manually set to 4.5 m/s by cross referencing the PWM signal applied to the tunnel motor with the pitot tube attached to the test section. Data collection began approximately 30 seconds after the wind tunnel speed was set to allow the turbine system to reach steady state. Once the data had been recorded, the wind tunnel was set to the next highest speed in the test progression. The process was repeated until the 8 m/s case was completed.

Once the final test for the forward progression stage was completed, the reverse progression stage began. Without turning the wind tunnel off, the wind velocity was set from 8 m/s to 7 m/s. The tests were conducted in a similar manner to the forward progression tests where the turbine was allowed to reach steady state and then data was

recorded for four minutes. The next lowest wind speed was then set and the process repeated until the 4.5 m/s case had been conducted. The wind tunnel is then turned off and the preparation phase of the next test began.

4.1.2 Optimal Configuration Results

The overall efficiency of the system is a function of the tip speed ratio of the rotor, the angular velocity of the generator, and the load impedance. The redesigned AGU was tested for a variety of load impedance values with 2:1, 3:1, and 4:1 gear ratios. As mentioned in Chapter 4.1.1, data for each test was collected for 4 minutes. A sample test is shown below to showcase a typical set of data (Figure 18). Results from the 2:1, 3:1, and 4:1 gear ratio configurations are shown below (Figures 19-21).

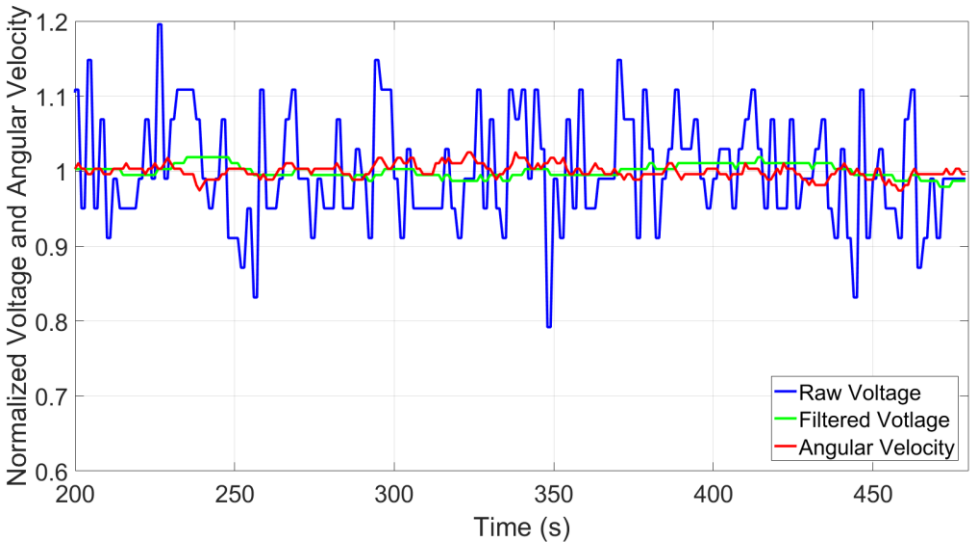

Figure 18: Example Test Data

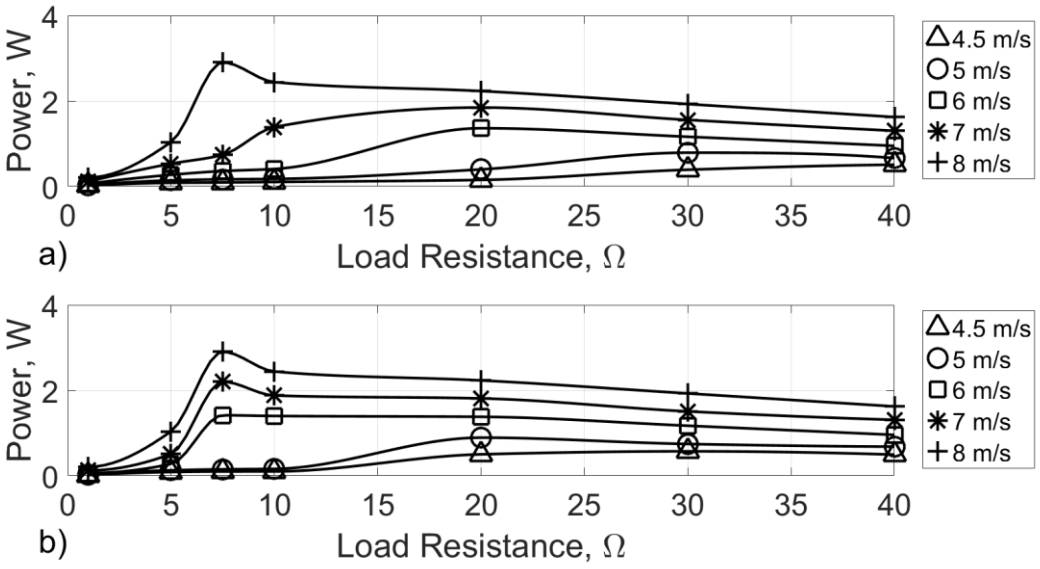

Figure 19: Power vs Load Resistance for the 2:1 Gear Ratio Configuration: a) Forward and b) Reverse

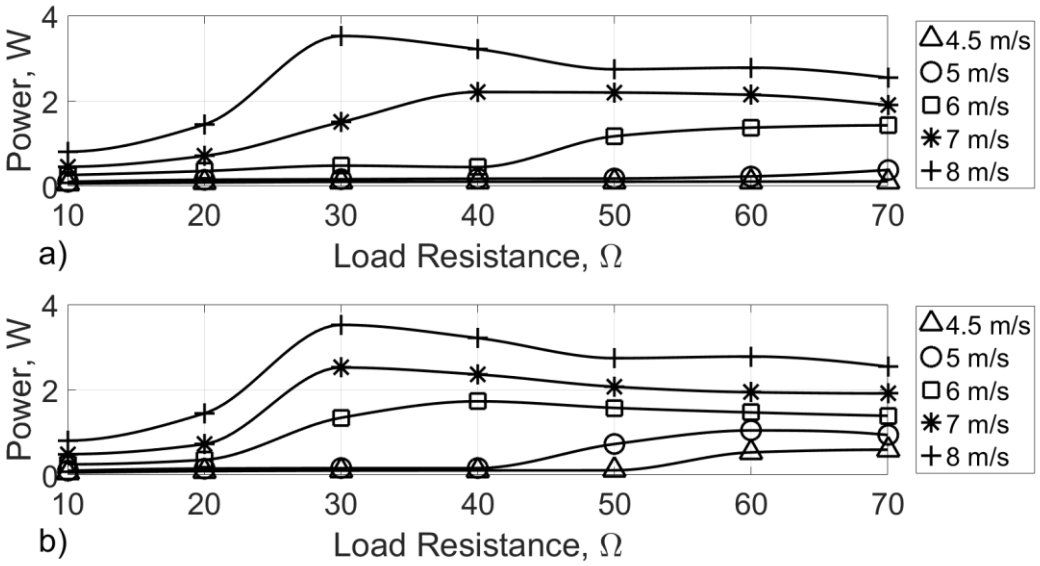

Figure 20: Power vs Load Resistance for the 3:1 Gear Ratio Configuration: a) Forward and b) Reverse

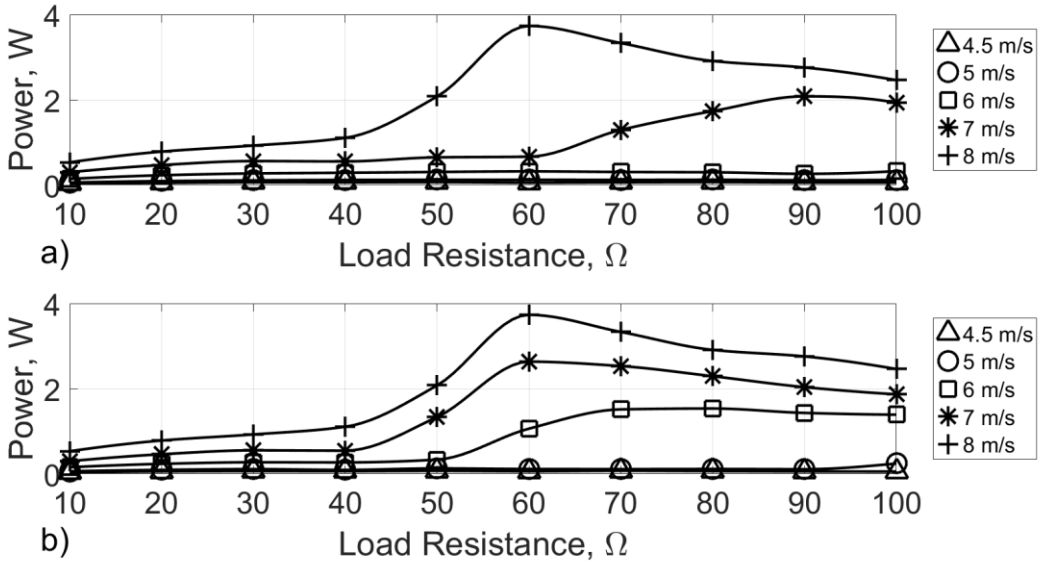

Figure 21: Power vs Load Resistance for the 4:1 Gear Ratio Configuration: a) Forward and b) Reverse

The results from each gear ratio configuration show that the generated power increases with wind speed without exception. It is also clear that the load resistance plays an integral part in determining the efficiency of the system, particularly when the load resistance allows the generator speed to "jump", or increase significantly with an increase in wind speed. The jump is a consequence of the lift and drag characteristics of the Clark-Y airfoil employed by the rotor. Due to the "jump" phenomenon, substantial hysteresis was observed throughout testing. That is, a different amount of power is obtained when the wind tunnel speed is swept from low speed to high speed as compared to a sweep starting at a high speed and progressing to lower speeds. This is clearly visible when contrasting parts a) and b) of Figure 19-Figure 21. In all cases, the power generated in the reverse

progression stage was greater than or approximately equal to the power generated in the forward progression stage. The physics behind the "jump" are further addressed in CHAPTER 5.

Figure 22 presents the two most power efficient impedance cases for each gear ratio to clearly showcase the optimal configuration of the system. Designing for a specific case, 6 m/s, the 3:1 gear ratio with 40 Ω load resistance is the most efficient producing 1.73 W, 2.36 W, and 3.21 W at 6, 7, and 8 m/s respectively.

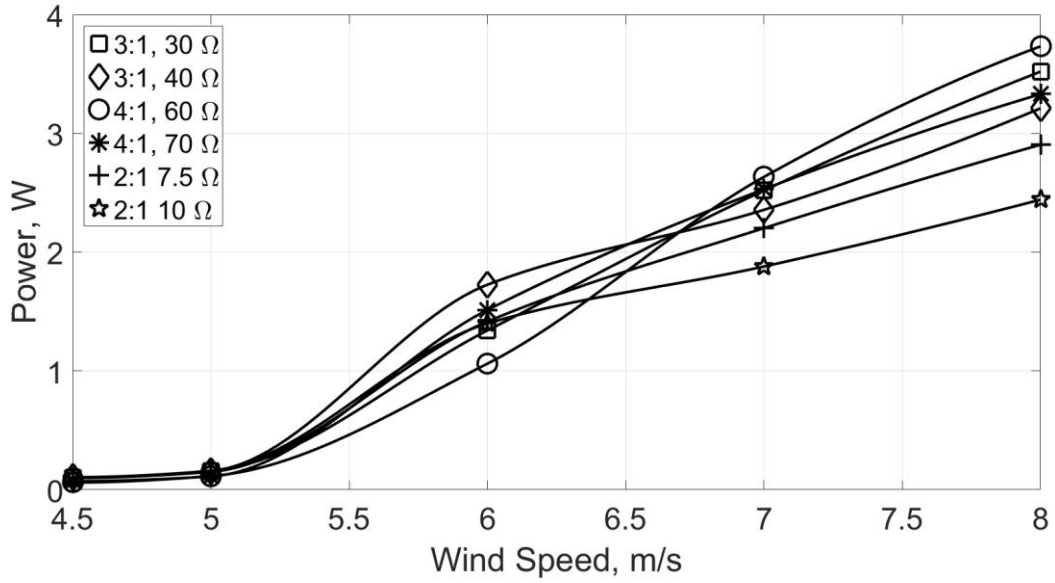

Figure 22: Power vs Wind Speed for the Optimal Impedance Cases of Each Gear Ratio

4.2 Power Analysis at Non-Optimum Relative Wind Angles

With the optimal configuration determined, the system must be examined under non-ideal conditions, namely different angles of relative wind. During flight, the AGU of the

guided airdrop system will rarely have a zero-degree relative wind angle, nevertheless the system must be able to provide sufficient power.

Tests were conducted to determine the effect of side slip angle and angle of attack on power generation. The non-optimum relative angle tests were directed in a similar manner to the optimal configuration tests. The only discrepancy between the two lies in the preparation phase where the side slip angle or the angle of attack were set in addition to the resistance value. To ensure greater accuracy, each test was conducted three times and the results were averaged. This mitigated the effect of error in the testing setup such as error in setting the side slip angle, angle of attack, or wind speed. Each test operated with a 3:1 gear ratio and a load impedance of 30 **Ω**.

Theoretically, for a non-ducted, ideal rotor the power should decrease by Eq. (26) where P_N is the nominal power at 0 degree angle of attack or side slip and α is the side slip angle or angle of attack. Equation (26) is a product of the degradation of the effective rotor area by the cosine of the angle.

$$P = P_N \cos(\alpha) \tag{26}$$

In Figure 23, plots of the power generated as a function of side slip and angle of attack are shown for constant wind speeds. Each marker represents a data point collected while the dashed lines represent the best-fit constant. The range of 0 to 15 degrees was analyzed due to the limited range of side slip angle or angle of attack that an AGU experiences during flight. In fact, most dynamic models of parafoil-payload systems model the AGU as rigidly attached to the parafoil, highlighting the minimal relative wind angles an AGU typically experiences [24].

It is evident from Figure 23 that the angle of side slip and the angle of attack has a minimal effect on generated power between 0 and 15 degrees. The cosine of 15 degrees is approximately 0.966. Reexamining Eq. (25), with a non-ducted ideal rotor, it would be expected that the power at the extreme angles would still be approximately 97% of the nominal power. This minimal difference is highlighted by the constant value best fit line.

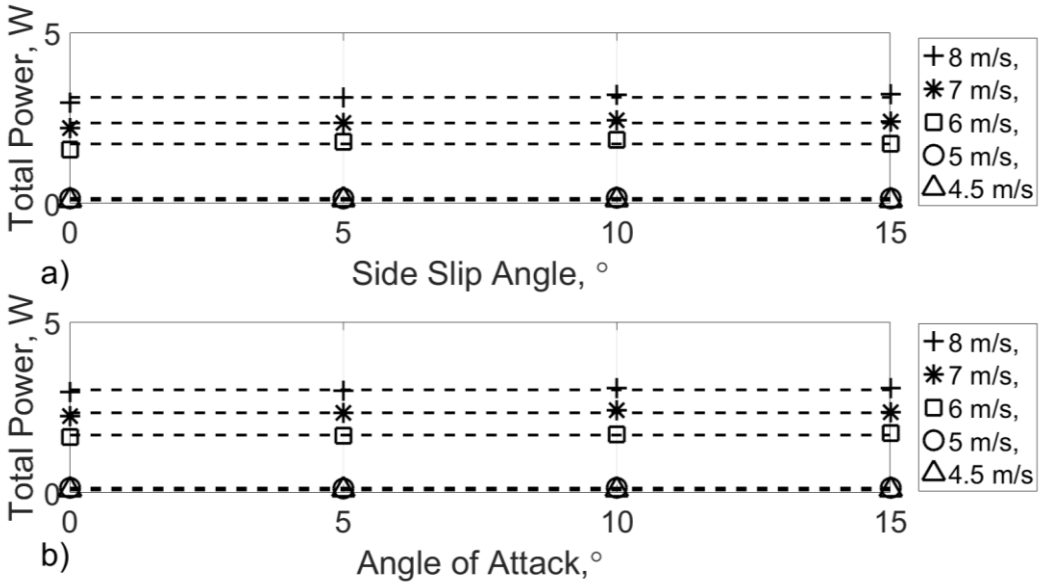

Figure 23: Power Variation vs Angle of Relative Wind with a Zero Order Polynomial Fit: a) Power vs Side Slip Angle and b) Power vs Angle of Attack

CHAPTER 5. ANALYSIS OF THE JUMP PHENOMENON

As mentioned in CHAPTER 4, the "jump" phenomenon is when the measured generator speed increases significantly with an increase in wind speed. This phenomenon is caused by the lift and drag characteristics of the Clark-Y airfoil, the airfoil employed by the rotor, as a function of tip speed ratio and thus the generated torque as a function of tip speed ratio.

The drastic increase in angular velocity noted in wind tunnel testing can be attributed to a sharp rise in the Lift/Drag coefficient at a tip speed ratio of approximately 1.5. Figure 24 shows the relationship between the angle of attack for each blade element as a function of tip speed ratio as well as a horizontal line indicating the angle of attack when the airfoil begins to stall. The lowest tip speed ratio which all the blade elements operate below stall is approximately 3.6.

Figure 25 displays each blade element's Lift/Drag coefficient as a function of tip speed ratio with a vertical line representing the lowest tip speed ratio where each section of blade is below stall (determined from Figure 24). This tip speed ratio corresponds not only to the maximum Lift/Drag coefficient, but also to the maximum coefficient of power.

The sharp increase in the Lift/Drag coefficient results in a significant increase in the torque produced by the rotor for a modest increase in angular velocity. Referring to Figure 5, as the tip speed ratio increases, the torque generated from the wind turbine has a steep ascent, reaches a maximum, and then descends almost linearly. The steep ascent leads to a rapid increase in generated torque which accelerates the rotor until a stable equilibrium point is reached.

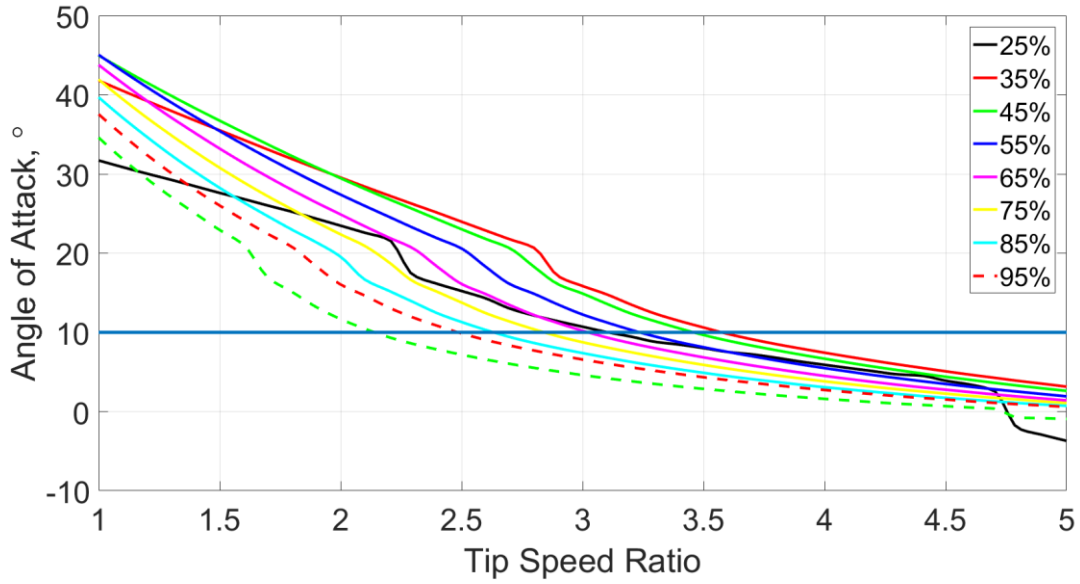

Figure 24: Angle of Attack vs Tip Speed Ratio for Each Blade Element

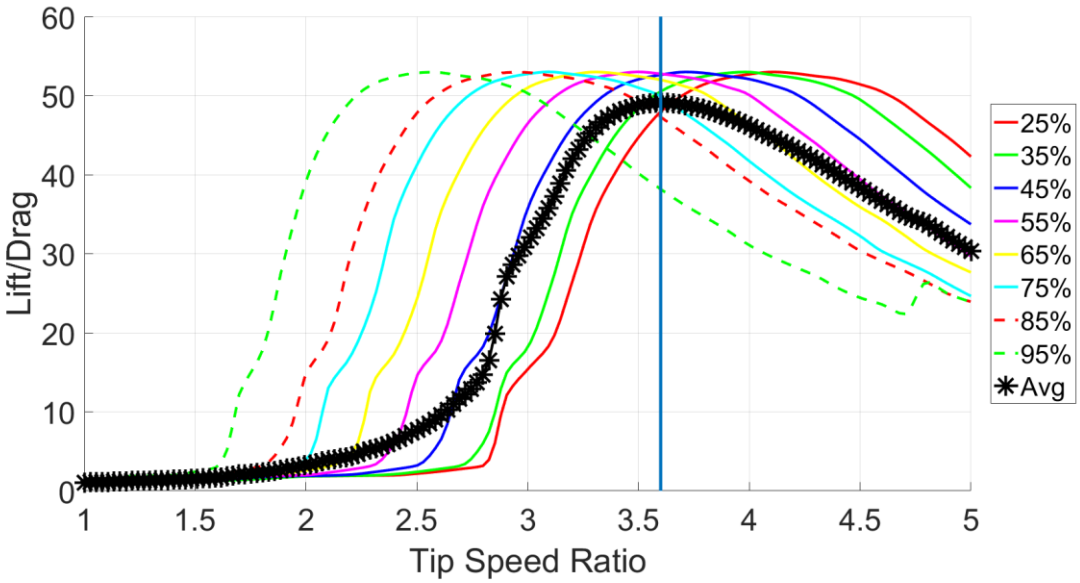

Figure 25: Lift/Drag vs Tip Speed Ratio for Each Blade Element

5.1 Mathematical Model of the Wind Turbine System

A two degree of freedom dynamic simulation was created to analyze the behavior of a coupled rotor, gear box, generator, and resistive load system in response to a time dependent wind stream. The simulation numerically integrates the equations of motion of the system using a standard RK4 method with a fixed time step of 0.0001 s. The two states being analyzed are the current being produced by the generator, *I*, and the rotor's angular velocity, ω. The equations of motion for this system are represented by Eqs. (27)- (30).

$$\dot{\boldsymbol{x}} = [A]\boldsymbol{x} + \boldsymbol{B}u \tag{27}$$

$$\boldsymbol{x} = \begin{bmatrix} I \\ \omega \end{bmatrix} \tag{28}$$

$$A = \begin{bmatrix} -\dfrac{R_a + R_L}{L_a} & \dfrac{\eta R}{L_a K_v} \\ -\dfrac{K_t R}{J_1 + J_2 R^2} & -\dfrac{b_1 + b_2 R^2}{J_1 + J_2 R^2} \end{bmatrix} \tag{29}$$

$$\boldsymbol{B} = \begin{bmatrix} 0 \\ \dfrac{1}{J_1 + J_2 R^2} \end{bmatrix} \tag{30}$$

Where **u** is the generated torque from the rotor. The parameters used in the simulation are defined in Table 3. In addition, the value of each parameter used in simulation is provided.

The value of input torque used in the simulation was derived from the blade element momentum theory method outlined in CHAPTER 2. With knowledge of the free stream

wind velocity, the rotor radius, and the current angular velocity of the rotor, the tip speed ratio can be calculated according to Eq. (1). Utilizing the free stream velocity and the tip speed ratio, the corresponding generated torque value can be obtained using a look up table in the derivative function. A similar method is used to calculate the efficiency of the generator. Using the data associated with Figure 8 andFigure 9, a lookup table can be created to cross reference the load resistance of the electrical output and the angular velocity of the motor shaft to determine the efficiency of the generator.

Table 3: Wind Turbine Simulation System Parameters

Parameter Symbol	Description	Value
b_1	Damping Coefficient of Rotor	0 $s(Nm)^{-1}$
b_2	Damping Coefficient of the Generator	04.2e-5 $s(Nm)^{-1}$
J_1	Moment of Inertia of the Rotor	0.01 kgm^2
J_2	Moment of Inertia of the Generator	0.01 kgm^2
K_t	Generator Torque Constant	4.9e-4 $Nm(A)^{-1}$
K_v	Generator Speed Constant	1.93e4 $rpm(V)^{-1}$
L_a	Armature Inductance	14 mH
η	Generator and Gear Efficiency	---
R	Gear Ratio	2
R_a	Armature Resistance	6.7 Ω
R_L	Load Resistance	20 Ω

5.2 Simulation Results and Analysis

Two separate cases will be analyzed to observe the "jump" phenomenon. The first case will be to explore how the system responds when the free stream wind velocity starts at a low speed and is increased and the second case will examine the system's response when the wind speed starts high and is decreased.

The first case to be examined is the increasing wind speed case (Figure 26). In this simulation, the wind speed began at 5 m/s, increased to 6 m/s at a third of the total time, and then increased to 7 m/s at two thirds of the total time. The wind speed changes are highlighted with the vertical red line.

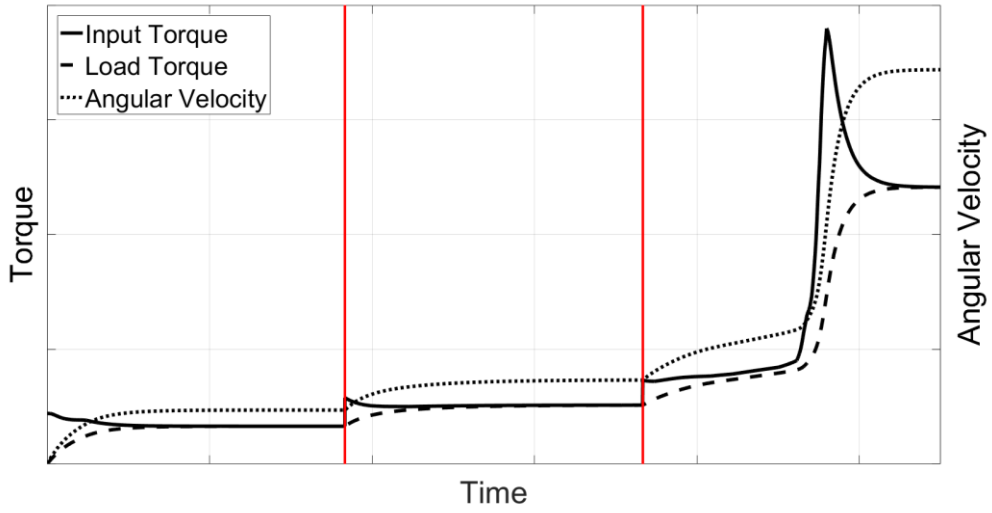

Figure 26: Simulated Values of Generated Torque, Load Torque, and Rotor Angular Velocity for the Increasing Wind Speed Case

Figure 26 shows the progression of the generated torque, load torque, and rotor angular velocity as a function of time for varying wind speeds. The two significant instances to highlight are when the two wind speed changes occur. When the wind speed changes from 5 to 6 m/s, there is a modest increase in the amount of generated torque in the system. This increase in generated torque causes a slight increase in speed eventually leading to a steady state solution well before the jump. However, when the wind speed increases from 6 to 7 m/s, the modest increase in generated torque causes the rotor to accelerate towards the beginning of the steep ascent of the generated torque versus tip speed ratio plot (Figure 5). Once the tip speed ratio reaches this value, the generated torque increases significantly faster than the load torque causing the jump phenomenon. The increase in tip speed ratio for the increasing wind speed case can be seen in Figure 27.

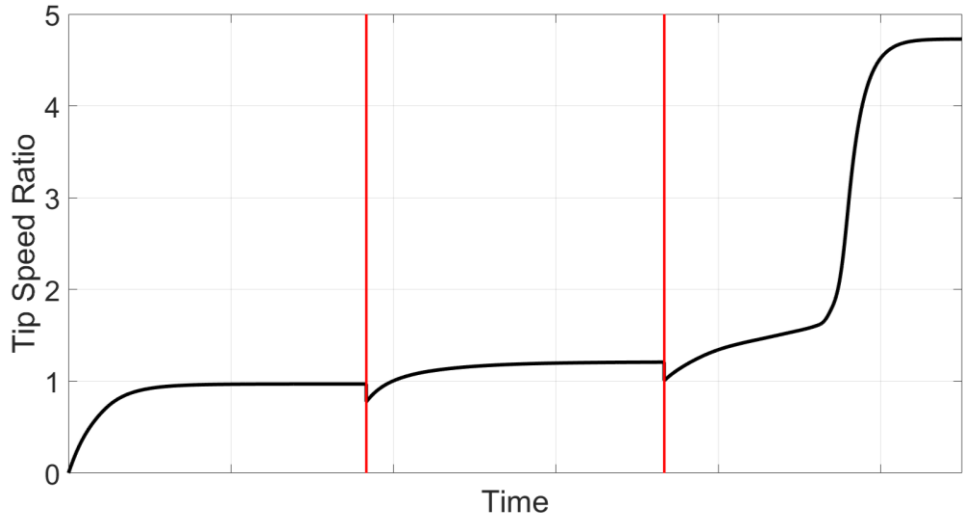

Figure 27: Simulated Tip Speed Ratio vs Time for the Increasing Wind Speed Case

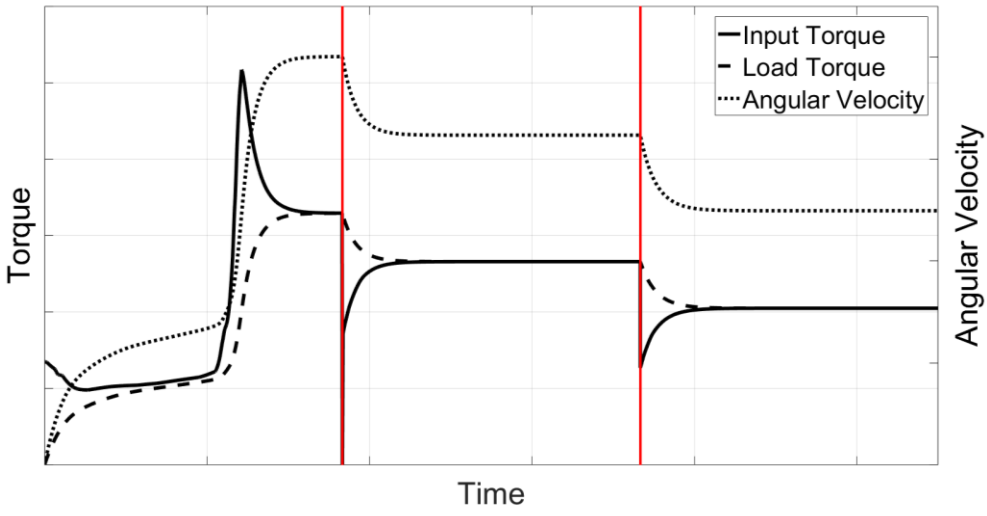

Figure 28: Simulated Values of Generated Torque, Load Torque, and Rotor Angular Velocity for the Decreasing Wind Speed Case

The second simulated case highlights the reverse of the jump phenomenon, when the wind speed starts at a high value and progresses to a lower value. In this simulation, the wind speed began at 7 m/s, was decreased to 6 m/s after one third of the total time, and was decreased to 5 m/s for the final third of the total time. The results of the generated torque, load torque, and rotor angular velocity are shown in Figure 28.

During the first third of the simulation, the rotor begins from rest and increases in rotational velocity until the jump occurs. When the wind speed is decreased from 7 m/s to 6 m/s, the rotor rotational velocity decreases by a small amount. The important feature in the simulation is when the wind speed is decreased from 6 m/s to 5 m/s. The steady-state angular velocity of the rotor at 5 m/s is three times faster for the decreasing wind speed case than the increasing wind speed case. This proves that there are two stable equilibrium points of the system for a given wind speed.

The trend of the steady-state angular velocity being greater for the decreasing wind speed case than the increasing wind speed case would be expected to continue until decreasing the tip speed ratio results in a decrease in torque. Examining Figure 28, when the wind speed is suddenly decreased, either from 7 to 6 m/s or 6 to 5 m/s, the generated torque from the rotor initially decreases. This is due to the immediate effect of switching between two different constant wind speed lines in the torque versus tip speed ratio curve (Figure 5). However, as the angular velocity of the rotor begins to decrease, the generated torque increases. This is due to the rotor moving to the maximum producible torque value. Once the rotor's tip speed ratio reaches the maximum torque value, 3.0, the input torque will no longer increase to meet the load torque. This will result in the system stabilizing about its equilibrium point to the left of the maximum.

5.3 Aerodynamic Jump Trade Study

In addition to determining how the system behaves with changes in wind speed, it is also valuable to observe the effect that changing various parameters can have on the system's response. Trade studies were conducted to visualize the effect that changing load impedance, friction, and inertia had on the system.

As mentioned in CHAPTER 4, the load impedance seen by the generator is a crucial parameter to vary to maximize efficiency. A simulation was conducted which analyzes the rotor system with a gear ratio of 2:1 at a wind speed of 7 m/s to determine the effect that load impedance has on efficiency. Figure 29 displays how the tip speed ratio of the system changes with a change in load impedance. For lower impedance values, the system's response to the sudden wind speed is slower than higher impedance values. Additionally, the steady-state value for low impedance values is less than that of high impedance values. This can be seen more clearly in Figure 30. This trend is corroborated by Figure 31 which displays the input torque generated by the rotor as well as the load torque for each configuration. The load torque for the low impedance values is higher than for the large impedance values because of the greater back EMF being generated. This finding is intuitive as the generator has the greatest amount of load torque, thus rotates slowest, when the leads of the generator are short circuited and rotates the fastest when the leads are in an open circuit configuration and no current can flow.

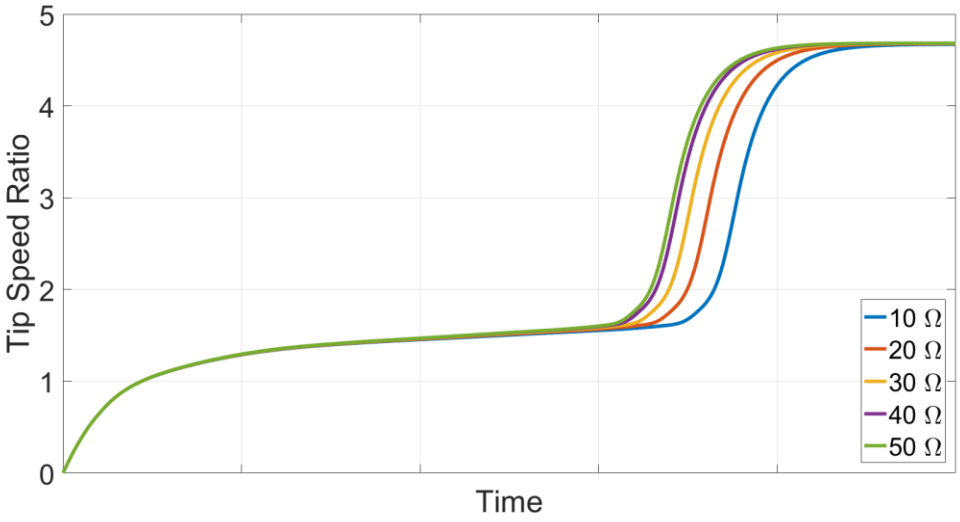

Figure 29: Simulated Tip Speed Ratio vs Time for a 2:1 Gear Ratio Configuration at a Wind Speed of 7 m/s for Varying Load Impedance Values

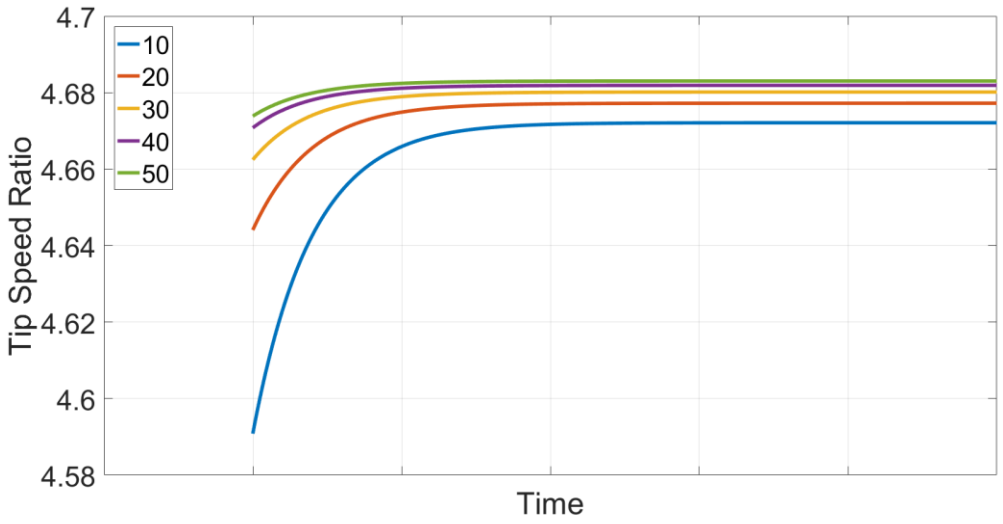

Figure 30: Steady-State Tip Speed Ratio Values for a 2:1 Gear Ratio Configuration at a Wind Speed of 7 m/s for Varying Load Impedance Values

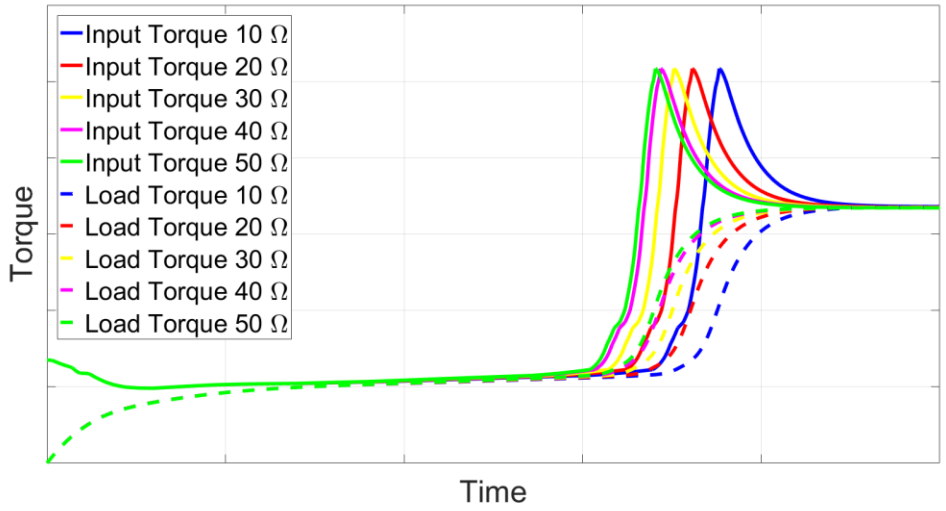

Figure 31: Simulated Input Torque and Load Torque for a 2:1 Gear Ratio Configuration at a Wind Speed of 7 m/s for Varying Load Impedance Values

Another critical parameter is the friction in the system. Figure 32 displays the system's response to changes in the friction in the bearings and gearbox. As the friction increases, the system's response slows down. This becomes crucial when the friction in the system is increased to a point where the tip speed ratio of the rotor is no longer large enough to induce the jump phenomenon. Another interesting result made apparent by Figure 33, is that the steady-state torque value of the system is greater for a normalized friction coefficient of 1.0 than it is for the 0.8 or 0.9 cases. Reexamining this result with Figure 5, the generated torque reaches a maximum at a tip speed ratio of 3.0 and then begins to decrease. For the 0.8 and 0.9 cases, the tip speed ratios increase past the maximum point, causing the generated torque to decrease. This highlights the importance of correctly configuring the system parameters to operate at the maximum efficiency.

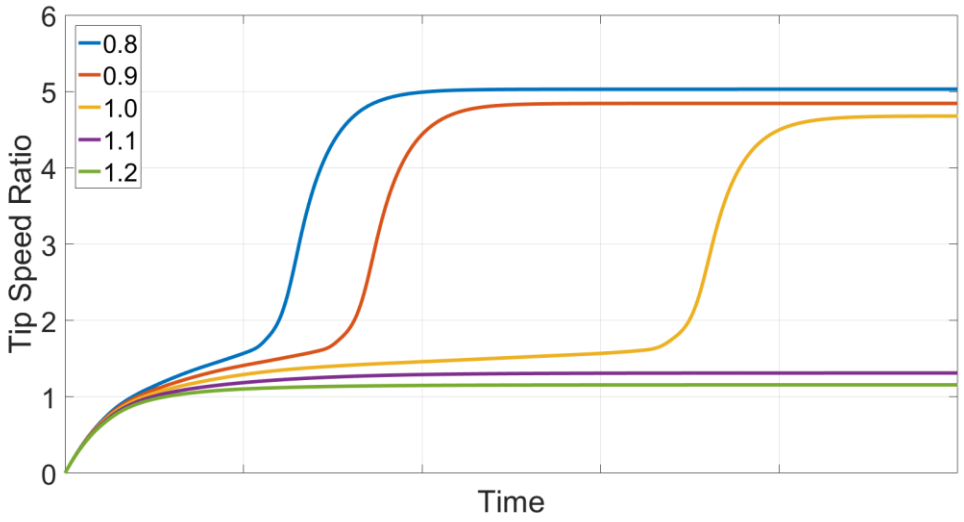

Figure 32: Simulated Tip Speed Ratio vs Time for a 2:1 Gear Ratio Configuration at a Wind Speed of 7 m/s for Varying Normalized Friction Values

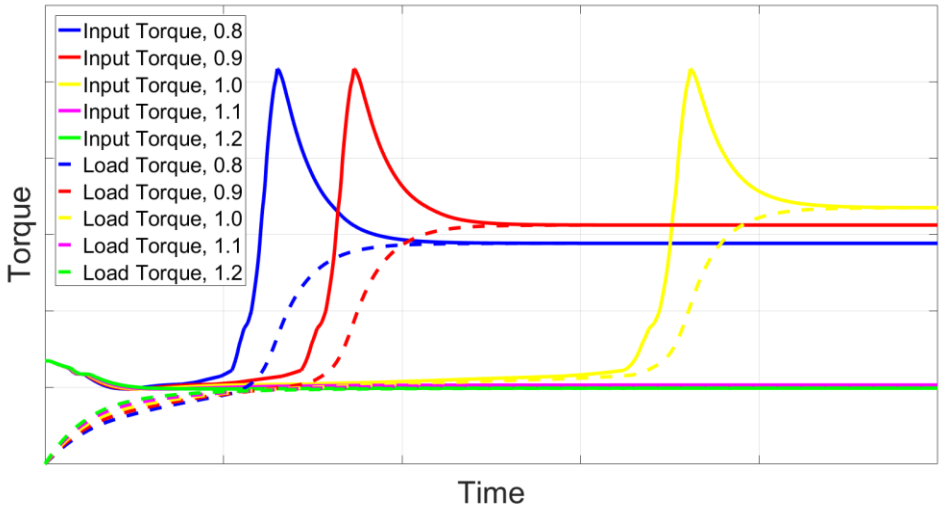

Figure 33: Simulated Input Torque and Load Torque for a 2:1 Gear Ratio Configuration at a Wind Speed of 7 m/s for Varying Normalized Friction Values

The last parameter examined in the trade study is the inertia of the generator subsystem. Both FiguresFigure 34 andFigure 35 show that the generator inertia does not impact the steady-state angular velocity of the rotor, rather the increase in inertia simply slows the system's rise time. This study also noticed similar trends when the rotor's inertia was analyzed, where an increase in inertia led to a slower rise time. This is due to the equations of motion of the system. The effect of increasing either the rotor or generator's inertia is simply to increase the overall inertia of the system.

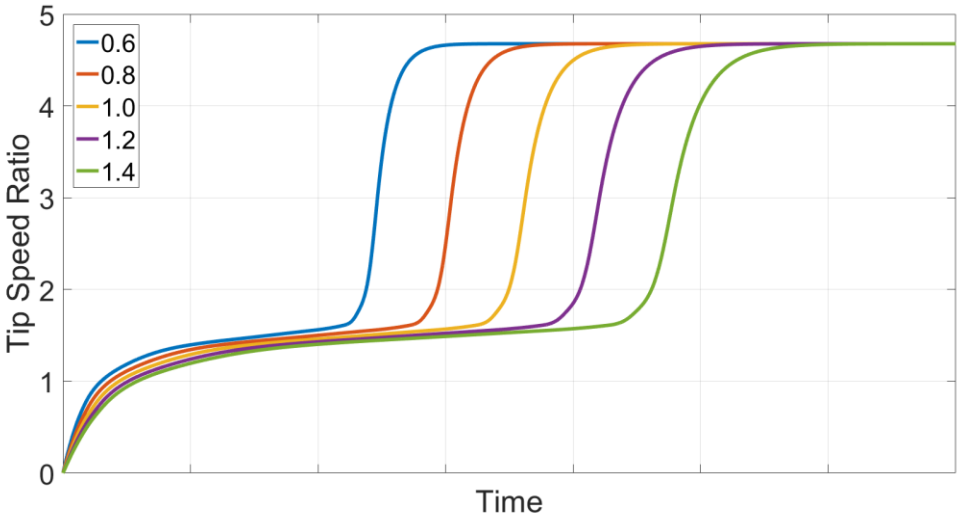

Figure 34: Simulated Tip Speed Ratio vs Time for a 2:1 Gear Ratio Configuration at a Wind Speed of 7 m/s for Varying Normalized Generator Inertia Values

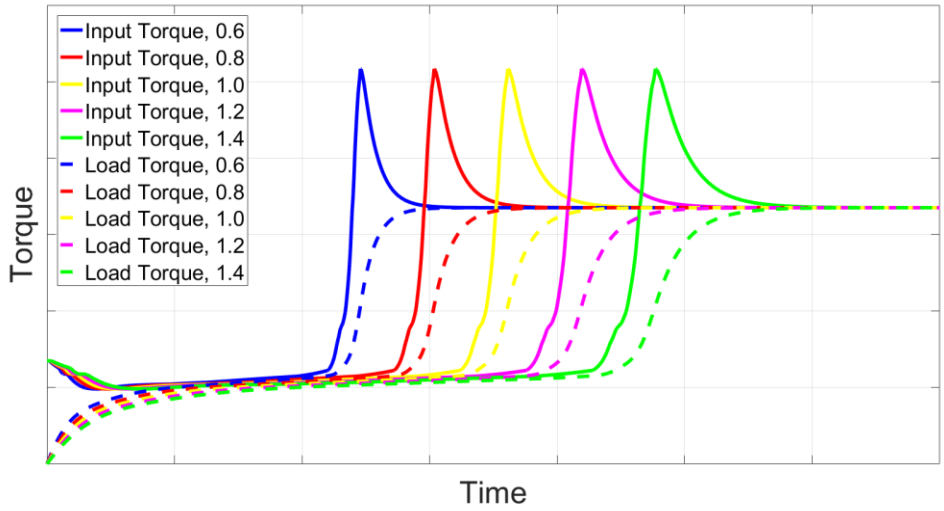

Figure 35: Simulated Input Torque and Load Torque for a 2:1 Gear Ratio Configuration at a Wind Speed of 7 m/s for Varying Normalized Generator Inertia Values

5.4 Theoretical Control Scheme

Due to the jump phenomenon, there is significant hysteresis in wind turbine operation. For the turbine to be most effective, it is critical that the turbine operates after the jump occurs. The jump can be initiated by controlling the load resistance of the electrical circuit; the higher the resistance, the less load torque is applied to the rotor thus, a lower wind speed is required to initiate the jump. This is intuitive as the load torque produced by the generator is greatest when the leads of the motor are short circuited and least when there is an open circuit. For the practical range of wind speeds seen by lightweight parafoil-payload aircraft, it is possible to increase the resistance to a point where the jump will occur.

This finding leads to the notion that a controller can be implemented to ensure that the turbine is always operating to the right of the maximum torque point. At the beginning of the flight, the load impedance of the system would be increased so that the rotor operated on the right side of the maximum torque value. A gradient based method can then be implemented such that the impedance value would be decreased until a decrease in impedance resulted in a decrease in efficiency.

CHAPTER 6. CONCLUSION

A full-scale energy harvesting system was successfully designed, fabricated, and tested in a wind tunnel. The results from the testing indicate that a modestly sized AGU with a rotor diameter of 0.33 m is able to provide over 3.7 W of power at a wind speed of 8 m/s. According to data logged from a typical bleed air controlled flight, the average power required for controls and actuation is approximately 1.5 W.[1] Even at the slowest typical wind speeds, the wind turbine system is able to provide sufficient power to the system. In addition, it was determined that when operating at a non-optimum relative wind angle within the range of typical angles of attack and sideslip, the power being produced from the turbine is not significantly diminished.

Furthermore, the jump phenomenon observed during wind tunnel testing was modelled and simulated to understand the underlying physics. The jump was determined to be caused by the Lift/Drag ratio of the Clark-Y airfoil, the airfoil employed by the rotor, as a function of tip speed ratio. The very sharp increase in this ratio causes the generated torque to drastically increase with a slight increase in rotor angular velocity. This leads to significant hysteresis in the system meaning that a different amount of power is generated when the wind speed is swept from high wind speeds to low wind speeds as compared to a sweep beginning at a low wind speed progressing to higher speeds. This phenomenon was observed to be vital in the successful implementation of a wind energy harvesting mechanism onboard a guided airdrop system as the power generated by a system being swept from high wind speeds to low wind speeds produces significantly more power.

[1] Per personal communication.

REFERENCES

[1] Benney, R., Barber, J., McGrath, J., McHugh, J., Noetscher, G., and Tavan, S., "The Joint Precision Airdrop System Advanced Concept Technology Demonstartion," *AIAA Paper 05-1601*, 2005.

[2] Benney, R., Henry, M., Lafond, K., Meloni, A., and Patel, S., "DoD New JPADS Programs & NATO Activities," AIAA Paper 09-2952 , 2009.

[3] George, S., Carter, D., Berland, J. C., Dunker, S., Tavan, S., and Barber, J., chap. The Dragonfly 4,500 kg Class Guided Airdrop System, Infotech@Aerospace Conferences, American Institute of Aeronautics and Astronautics, Sep 2005.

[4] Simpson, C., "Characteristics of Rechargeable Batteries," Tech. rep., Texas Instruments, 2011.

[5] Hebert, C., Cowan, D., Peter, A., and Weiseman, C., "Aeroelastic Flutter," AIAA database [online database], URL: http://dl.btc.pl/kamami_wa/hk_24474_2.pdf [cited 01 March 2017].

[6] Manivannan, V., and Costello, M., "Wind Energy Extraction Using a Wind Fin," Georgia Institute of Technology, School of Aerospace Engineering.

[7] Ward, L., "Windbelt, Cheap Generator Alternative, Set to Power Third World," *Popular Mechanics,* Popular Mechanics, 25 Mar. 2015.

[8] Sivadas, V., and Wickenheiser, A, M., "A Study of Several Vortex-Induced Vibration Techniques for Piezoelectric Wind Energy Harvesting," *Proceedings of SPIE-The International Society for Optical Engineering,* Vol. 7977 79770F, Mar. 2011.

[9] Lee, C., Liu, J., Liu, H., Yang, B., *Micro and Nano Energy Harvesting Technologies,* Boston, Artech House, 2015.

[10] Bae, J. et al., "Flutter-Driven Triboelectrification for Harvesting Wind Energy," *Nature Communications 5,* No. 4929, 2014.

[11] Federspiel, C. C., and Chen, J., "Air-Powered Sensor," *Sensors, 2003, Proceedings of IEEE,* Vol. 1, Oct. 2003, pp. 22-25.

[12] Rancourt, D., Tabesh, A., and Frechette, L., "Evaluation of Centimeter-Scale Micro Wind Mills: Aerodynamics and Electromagnetic Power Generation," Proceedings Power MEMS, Nov. 2007, pp. 93-96.

[13] Xu, F. J., Yuan, F.G., Hu, J.Z., and Qiu, Y. P., "Design of a Miniature Wind Turbine for Powering Wireless Sensors," 2010.

[14] Holmes, A. S., Hong, G., Pullen, K. R., "Axial-Flux Permanent Magnet Machines for Micropower Generation," *Journal of Microelectromechanical Systems* 14.1, 2005, pp. 54-62.

[15] Hirahara, H., Hossain, M. Z., Kawahashi, M., and Nonomura, Y., "Testing Basic Performance of a Very Small Wind Turbine Designed for Multi-Purposes," *Renewable Energy 01/2005,* Jan. 2005.

[16] Priya, S., "Modeling of Electric Energy Harvesting Using Piezoelectric Windmill," *Applied Physics Letters,* Vol. 87, No. 18, Oct. 2005, pp. 1838-1844.

[17] Carli, D., Brunelli, D., and Benini, L., "A high-efficiency wind-flow energy harvester using micro turbine," *Power Electronics Electrical Drives Automation and Motion (SPEEDAM),* 2010 International Symposium on Jun. 2010, pp. 778-783.

[18] Sardini, E., and Sprpelloni, M., "Self-Powered Wireless Sensor for Air Temperature and Velocity Measurements With Energy Harvesting Capability," *Instrumentation and Measurement, IEEE Transactions on,* Vol. 60, No. 5, May 2011, pp. 1838-1844.

[19] Danick, B., Yeatman, E., Roundy, S., Brand, O., Fedder, G, K., Hierold, C., Korvink, J, G., and Tabata, O., *Micro Energy Harvesting,* Weinheim: Wiley-VCH, 2015, pp. 316-317.

[20] Huleihil, M., and Mazor, G., chap. Wind Turbine Power: The Betz Limit and Beyond, Advances in Wind Power, InTech, 2012.

[21] Manwell, J. F., McGowan, J. G., Rogers, A. L., *Wind Energy Explained: Theory, Design and Application,* 2nd ed., John Wiley and Sons, Chichester, U.K., 2009, pp.137-137.

[22] Eggleston, D. M., and Forrest, S., *Wind Turbine Engineering Design,* Van Nostrand Reinhold, New York, 1987.

[23] Miley, S.J., "A catalog of Low Reynolds Number Airfoil Data for Wind Turbine Applications,"United States Department of Energy, Wind Technology Division, RFP-3387, UC-60, Texas A&M University, College Station, TX, 1982.

[24] Slegers, N. J., "Comparison of Parafoil Dynamic Modes with Varying Payload Connections." *AIAA Aerodynamic Decelerator Systems Technology Conference,* AIAA, Denver, CO., 2017.